Journal of Volcanology and Geothermal Research 438 (2023) 107821

Contents lists available at ScienceDirect

Journal of Volcanology and Geothermal Research

journal homepage: www.journals.elsevier.com/journal-of-volcanology-and-geothermal-research

# Elucidating the magma plumbing system of Ol Doinyo Lengai (Natron Rift, Tanzania) Using satellite geodesy and numerical modeling

Ntambila Daud [a,b,*], D. Sarah Stamps [a], Maurizio Battaglia [c,d], Mong-Han Huang [e], Elifuraha Saria [b], Kang-Hyeun Ji [f]

[a] Virginia Tech, Department of Geosciences, Blacksburg, VA, USA
[b] Ardhi University, Dar Es Salaam, Tanzania
[c] U.S. Geological Survey, Volcano Disaster Assistance Program, Moffett Field, CA, USA
[d] Sapienza - University of Rome, Department of Earth Sciences, Rome, Italy
[e] University of Maryland, College Park, MD, USA
[f] Korea Institute for Geoscience and Mineral Resources, Daejeon, South Korea

ARTICLE INFO

*Keywords:*
TZVOLCANO
dMODELS
GNSS
InSAR
Ol Doinyo Lengai
Magma plumbing system

ABSTRACT

Ol Doinyo Lengai, located in the southern Eastern Branch of the East African Rift had several eruptive episodes with ash falls and lava flows (VEI 3) that caused damage to the nearby communities between 2007 and 2010. The volcano is remote and access is difficult. Although this volcano has been studied for decades, its plumbing system is still poorly understood, in part, because of the lack of precise observations of surface deformation during periods of quiet and unrest. This study investigates the volcanic plumbing system of Ol Doinyo Lengai and its surroundings using data from the network of permanent Global Navigation Satellite System (GNSS) sites monitoring the volcano (the TZVOLCANO network) around the flanks of the volcano and Interferometric Synthetic Aperture Radar (InSAR) observations. We constrain surface motions using 6 GNSS sites distributed around Ol Doinyo Lengai, operating between 2016 and 2021, and InSAR data covering nearly the same time period. Because of the complex local tectonics, the interpretation of the deformation pattern is not straightforward. We first invert the GNSS deformation and InSAR observations independently to infer potential deformation sources. Then we perform a joint inversion of both GNSS and InSAR datasets to verify our findings. We compare the results from the joint inversion with the results from inverting each dataset independently. The GNSS, InSAR, and joint inversion results point to a deflating source, located east of Ol Doinyo Lengai and southwest of the dormant volcano Gelai at a depth of 3.49 ± 0.03 km (GNSS inversion), 5.2 ± 1.2 km (InSAR inversion) and 3.49 ± 0.06 km (joint inversion) relative to the summit (vent) and with a volume change ΔV of −0.04 ± 0.05 × $10^6$ $m^3$ (GNSS inversion), −0.39 ± 0.29 × $10^6$ $m^3$ (InSAR inversion), and − 0.04 ± 0.01 × $10^6$ $m^3$ (joint inversion). Although this is non-unique modeling of geodetic datasets with small signals, the inversion results suggest that Ol Doinyo Lengai could be fed by an offset multi-reservoir system that includes a shallow magma reservoir (<5 km) east of Ol Doinyo Lengai, possibly connected to a deeper magma reservoir.

## 1. Introduction

Volcanic processes and eruptions are governed by the magmatic plumbing system of the volcano, which is a series of interconnected networks of magma storage regions and feeder intrusions that transport magma from a source at depth to the Earth's surface (Burchardt and Galland, 2016; Murcia et al., 2019; Magee et al., 2018; Reiss et al., 2022). Magma channels usually start either in the asthenosphere or lithosphere and link to shallower conduit components such as dikes, sills, and magma reservoirs in the crust (Jerram and Bryan, 2015; Murcia et al., 2019). The plumbing system sets the eruption stage, controls the style, occurrences of an eruption, as well as the magnitude of eruptive activity that may result in monogenetic or polygenetic volcanoes. An understanding of magma plumbing systems, which we address in this work, and the physics of volcanic processes are key for effective volcanic monitoring and hazard mitigation. Characterizing the subsurface magma plumbing system is necessary to develop a volcanic risk assessment that can be used for community emergency response plans and

* Corresponding author at: Virginia Tech, Department of Geosciences, Blacksburg, VA, USA.
*E-mail address:* dntambila@vt.edu (N. Daud).

https://doi.org/10.1016/j.jvolgeores.2023.107821
Received 14 September 2022; Received in revised form 4 May 2023; Accepted 6 May 2023
Available online 13 May 2023

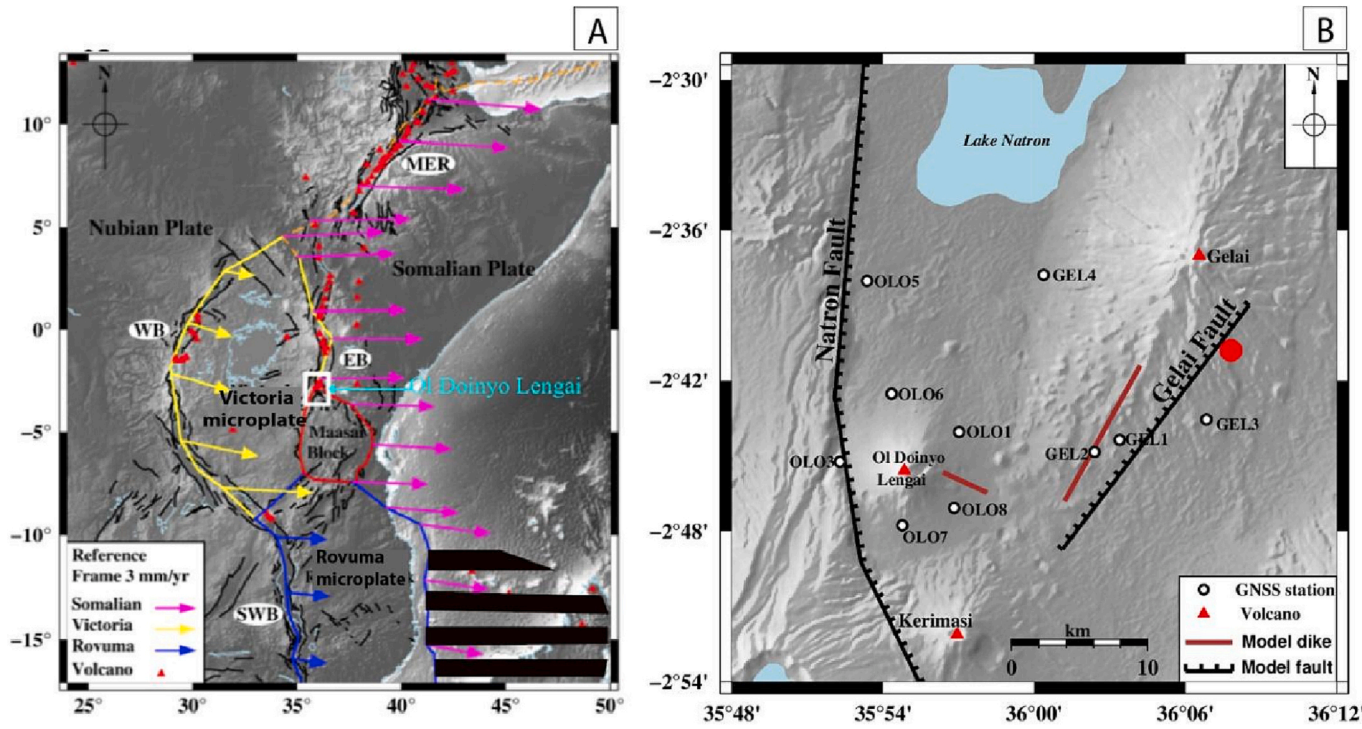


**Fig. 1.** Regional and local tectonics of Ol Doinyo Lengai. (A) The continental East African Rift, MER = Main Ethiopian Rift, WB = Western Branch (high seismicity and magma poor) EB = Eastern Branch (lower seismicity and magma rich) and SWB = southern Western Branch (higher seismicity and magma poor), black continuous line is the deforming zone (Stamps et al., 2021a, 2021b). (B). Simplified section of the Natron Rift. Faults are black lines with tick marks. Magma source near Gelai resolved by Biggs et al. (2009) is a circle in red and dikes are brown lines resolved during the 2007–08 episodic eruptions (Biggs et al., 2009, 2013). The active Ol Doinyo Lengai, the two dormant volcanoes, Gelai and Kerimasi (triangle in red) and the continuous GNSS stations (OLO1-OLO8) constituting the permanent TZVOLCANO network (white circles) monitoring the volcano installed in 2016. GEL1-GEL4 are campaign sites. (For interpretation of the references to colour in this figure legend, the reader is referred to the web version of this article.)

preparedness.

Ol Doinyo Lengai, located in the Natron Rift of the East African Rift (EAR; Fig. 1), is the only active volcano in the world known to erupt uncommon low-temperature carbonatites. The volcano is remote and access is difficult. The nearest unpaved road is several kilometers away from the area and the staff in charge of monitoring must hike for hours on uneven terrain to reach the volcano. The volcano has been very important to the growth of Tanzanian economy by attracting tourists from different parts of the world. At the same time, a better economy has encouraged the expansion of villages and communities around the volcano.

Global Navigation Satellite System (GNSS) and Interferometric Synthetic Aperture Radar (InSAR) observations are now standard techniques in monitoring volcanic deformation and are routinely applied to investigate volcanic plumbing systems (e.g., Sigmundsson et al., 1992; Newhall and Punongbayan, 1996; Dzurisin, 2006; Janssen, 2007; Wang and Wright, 2012; Wang et al., 2012; Segall, 2019; Battaglia et al., 2021a, 2021b). For example, GNSS and InSAR were employed to investigate ground motion at Arenal volcano in Costa Rica, improving the volcano monitoring thanks to better spatial and temporal coverage (Muller et al., 2015). The geological unrest of Yellowstone Caldera because of the migration of magma and hydrothermal fluids was quantified by integrating multiple measurements from InSAR, gravity, and leveling (Tizzani et al., 2015). Surface deformation constrained from InSAR and GNSS measurements inferred the magmatic source of a series of dike intrusions in 2005 at the Afar region in Ethiopia (Hamling et al., 2010). Modeling of subsidence measured by InSAR at Dallol volcano (Erta Ale Ridge, Afar) allowed for the inference of a deformation mechanism that was a combination of depressurization, cooling, and contraction of the roof of a shallow crustal magma chamber or of the hydrothermal system (Battaglia et al., 2021a, 2021b).

We use the TZVOLCANO GNSS network (Fig. 2) and InSAR data to investigate the geodetically detectable subsurface magma plumbing system of Ol Doinyo Lengai. It was politically and logistically quite difficult to set up the GNSS network. A memorandum of understanding was negotiated, remote satellite internet was set-up, and numerous educational efforts with the local community were undertaken to reduce vandalism of the stations. The TZVOLCANO network was established to monitor surface deformation at Ol Doinyo Lengai and fault slip on the adjacent Natron Fault. The network has four monitoring stations (OLO1, OLO6, OLO7, OLO8) installed on the flanks of the volcano Ol Doinyo Lengai, one station (OLO9, formerly OLO3) on the border fault (Natron Fault), one station (OLO5) outside the influence of the volcano to have a local reference station, and one co-located broadband seismic station at OLO6. The installation of these stations required substantial work by team members from Ardhi University, Korea Institute for Geoscience and Mineral Resources (KIGAM), Virginia Tech, Colgate University, and participants from the local Engaresero village. All stations are operated with remote power and are located away from major roads to obtain ideal positions relative to the volcano. The network observes and transmits low latency (daily files; Stamps et al., 2016a-e; Stamps et al., 2017a-c; Stamps et al., 2021a) and near real-time data (1 Hz data files; Stamps et al., 2016f) to UNAVCO with open access. All other data that are downloaded on-site are also made available for download at UNAVCO. The network detects horizontal and vertical motions and is poised to monitor precursory volcanic ground deformation, magma migration, and dike propagation. In section 3.1 we present a synthetic test that shows that the TZVOLCANO network provides sufficient coverage to invert for a spherical magma source.

Here, we hypothesize that an offset system with multiple magma reservoirs feeds Ol Doinyo Lengai (e.g., Baer et al., 2008; Reiss et al., 2021, 2022). We address this hypothesis by investigating the magma

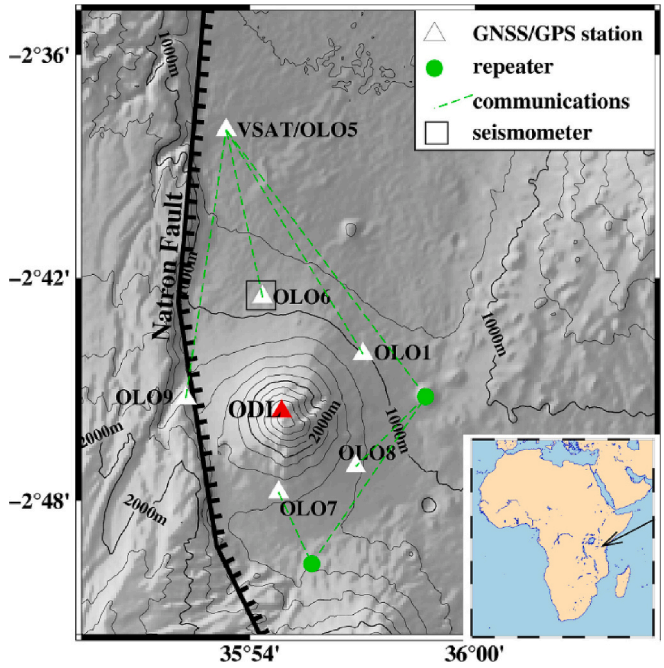


**Fig. 2.** The TZVOLCANO network (ODL = Ol Doinyo Lengai). White triangles are GNSS stations, the black, open square is a broadband seismometer, green circles are radio transmitters, dashed green lines are the communication pathways. The Natron Fault is depicted as a black line with tick marks indicating the downthrown side of this normal fault. The site OLO3 has been disassembled and replaced nearby with OLO9 (see Table 1 and Fig. 4). (For interpretation of the references to colour in this figure legend, the reader is referred to the web version of this article.)

plumbing system by inverting GNSS and InSAR data using the U.S. Geological Survey (USGS) code dMODELS (Battaglia et al., 2013a, 2013b) and a new joint inversion code. These approaches allow us to solve for different magma sources embedded in the crust. Compared to previous studies, we make use of GNSS data from the TZVOLCANO monitoring network that has never been published before.

This work suggests the existence of a shallow offset magma reservoir east of Ol Doinyo Lengai at a depth inferred by a previous petrological study (Petibon et al., 1998). Both GNSS and InSAR surface deformation show minor subsidence NE of the volcano that we can model as a shallow deflating point source. We are aware that the deformation data are noisy and do not present the kind of radial deformation pattern that we may expect from volcanic unrest (e.g., Cervelli et al., 2006). Nevertheless, we believe that much can still be learned even from the non-unique modeling of sparse and imperfect deformation data.

## 2. Tectonic and volcanic setting of Ol Doinyo Lengai

Ol Doinyo Lengai is in the north-south oriented Natron Rift adjacent to the Victoria microplate. The Gelai Fault is positioned to the east of the volcano (Fig. 1A, B). The Natron Rift extends eastward at ~3.8 mm/yr relative to the Nubian Plate (Stamps et al., 2021b). The Victoria microplate comprises the Tanzania Craton, which is reported to rotate counterclockwise and interact with the Natron Rift (Calais et al., 2006; Stamps et al., 2008; Fernandes et al., 2013; Saria et al., 2013, 2014). The Natron Rift is characterized by hallmark features of early phase magma-assisted rifting, dominated by active volcanism near the border faults with two dike intrusions in historical times near the center of the rift that did not reach the surface (Biggs et al., 2013) and a seismically resolved shallow region of melt filled fractures (Reiss et al., 2022). The rift exhibits high levels of low magnitude seismic activity, deep upper mantle thermal anomalies, and the youngest (and only) active carbonatitic volcano (e.g., Baer et al., 2008). To the east and north of the Ol Doinyo Lengai there are deep crustal seismic activities compared to the south and little seismicity has been detected directly below the volcano (Reiss et al., 2021). The presence of seismic activities occurring at mid to lower crustal depths is attributed to magmatic degassing or border fault extension and reflects the possible availability and movement of magmatic volatiles (Muirhead et al., 2020). However, seismic activity beneath the dormant Gelai volcano apparently has been changing over time since 2007 (Albaric et al., 2010; Weinstein et al., 2017; Reiss et al., 2021). Albaric et al. (2010) observed high seismic activity in the southern flanks beneath Gelai while Weinstein et al. (2017) detected seismic activity beneath the southern and western flanks of Gelai. Recently, Reiss et al. (2021) reported the seismic activity to have

**Table 1**
GNSS velocity solutions in the ITRF14 reference frame and relative to OLO5, as well as InSAR velocities relative to OLO5. The parameters, $V_E$, $V_N$, $V_U$, are the velocities in the east, north, and up directions, respectively. The parameters, $\sigma_E$, $\sigma_N$, $\sigma_U$, are the 1 sigma uncertainties on each component of the velocity. The parameter, $corr_{EN}$, is the correlation. Note that the InSAR velocities do not include N-S motions because they are not resolved.

| Site | Long | Lat | $V_E$ | $\sigma_E$ | $V_N$ | $\sigma_N$ | $corr_{EN}$ | $V_U$ | $\sigma_U$ | Years |
|---|---|---|---|---|---|---|---|---|---|---|
| | DD | DD | mm/yr | mm/yr | mm/yr | mm/yr | | mm/yr | mm/yr | |
| (a) GNSS velocity solutions (ITRF14) | | | | | | | | | | |
| OLO1 | 35.95 | −2.734 | 27.4 | 0.4 | 16.9 | 0.3 | 0.002 | −6.6 | 1.2 | 5 |
| OLO3 | 35.871 | −2.754 | 25.2 | 0.2 | 18.6 | 0.3 | 0.01 | −4.6 | 1.4 | 5 |
| OLO5 | 35.889 | −2.634 | 25.4 | 0.3 | 17.6 | 0.2 | −0.004 | −4.6 | 1 | 5 |
| OLO6 | 35.906 | −2.709 | 25.1 | 0.4 | 17.7 | 0.2 | −0.003 | −7.8 | 1.7 | 3.5 |
| OLO7 | 35.913 | −2.796 | 25.1 | 0.2 | 16.6 | 0.2 | −0.007 | −1.4 | 0.7 | 1.7 |
| OLO8 | 35.947 | −2.785 | 26 | 0.2 | 17.5 | 0.2 | −0.004 | −5.7 | 1.2 | 2.5 |
| (b) GNSS velocity solutions, relative to OLO5 | | | | | | | | | | |
| OLO1 | 35.95 | −2.734 | 2.0 | 0.4 | −0.7 | 0.3 | 0.002 | −2 | 1.2 | 5 |
| OLO3 | 35.871 | −2.754 | −0.2 | 0.2 | 1.1 | 0.3 | 0.01 | −0.1 | 1.4 | 5 |
| OLO6 | 35.906 | −2.709 | −0.3 | 0.4 | 0.1 | 0.2 | −0.003 | −3.3 | 1.7 | 3.5 |
| OLO7 | 35.913 | −2.796 | −0.3 | 0.2 | −1.0 | 0.2 | −0.007 | 3.1 | 0.7 | 1.7 |
| OLO8 | 35.947 | −2.785 | 0.6 | 0.2 | −0.1 | 0.2 | −0.004 | −1.2 | 1.2 | 2.5 |
| (c) InSAR velocity solutions, relative toOLO5 | | | | | | | | | | |
| OLO1 | 35.95 | −2.734 | −0.2 | 0.4 | – | – | – | −2.8 | 0.5 | 5 |
| OLO3 | 35.871 | −2.754 | 7.3 | 0.4 | – | – | – | −6.0 | 0.5 | 5 |
| OLO6 | 35.906 | −2.709 | 2.1 | 0.4 | – | – | – | −2.7 | 0.5 | 5 |
| OLO7 | 35.913 | −2.796 | −0.7 | 0.4 | – | – | – | −4.9 | 0.5 | 5 |
| OLO8 | 35.947 | −2.785 | −1.6 | 0.4 | – | – | – | −4.3 | 0.5 | 5 |

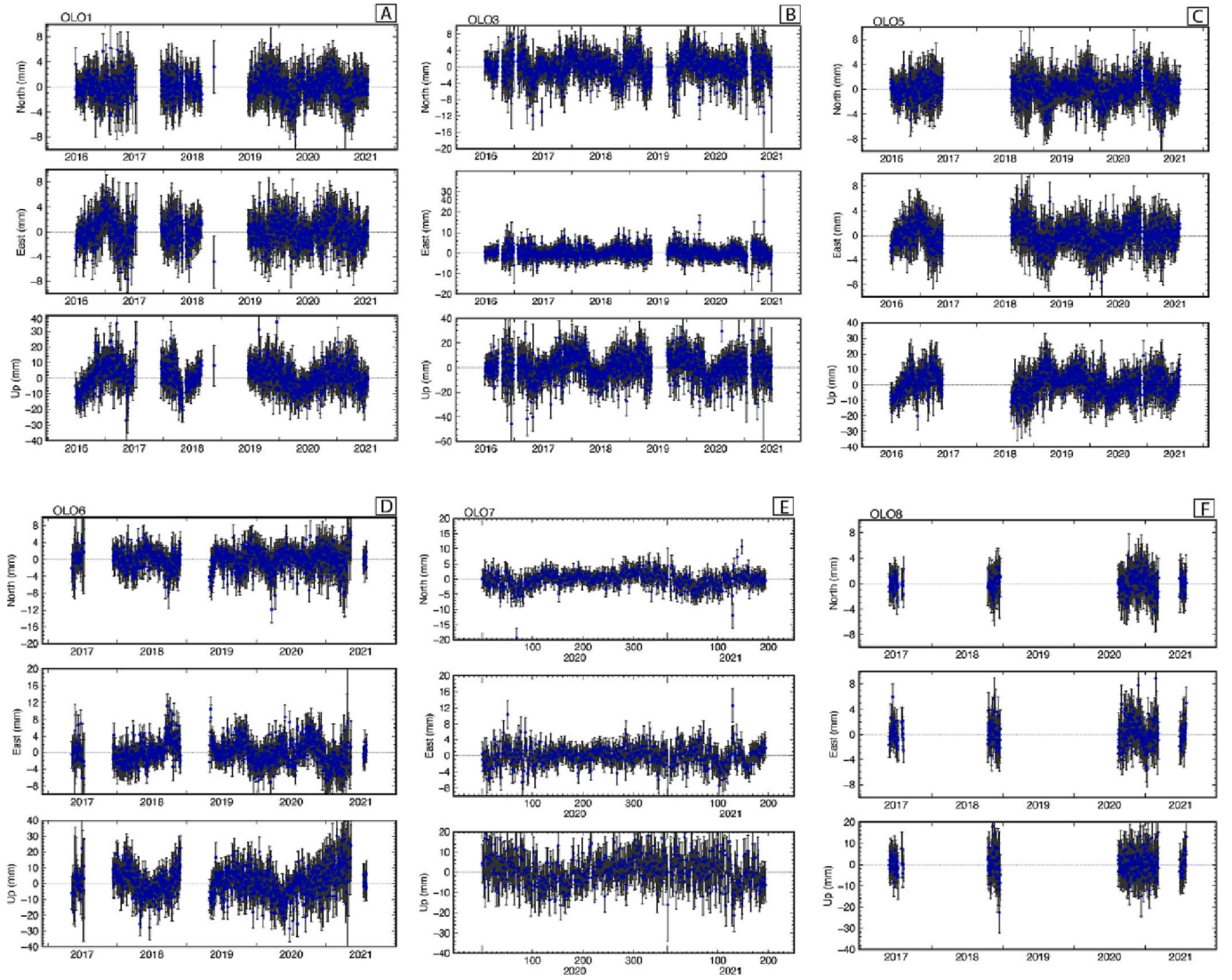


**Fig. 3.** Daily position time-series for the OLO1 (A), OLO3 (B), OLO5 (C), OLO6 (D), OLO7 (E), and OLO8 (F) sites (ITRF14 reference frame) with the mean secular velocity removed.

migrated northward, reaching the northern end of Gelai volcano, and Reiss et al. (2022) characterized an interconnected magma plumbing system beneath the Natron Rift. Both studies used arrays of temporary seismic instrumentation around the Natron Rift, the Ol Doinyo Lengai volcano, and the Gelai volcano.

Volcanic events that occurred in 2007–2008 at Ol Doinyo Lengai and surroundings were associated with tectono-magmatic activity. Numerous studies have associated these events with slip on the Gelai Fault and opening of the Gelai dike as commonalities (Calais et al., 2008; Baer et al., 2008; Biggs et al., 2009; Albaric et al., 2010; Biggs et al., 2013). Major differences arise in the magma reservoir locations and volume changes of the magma reservoirs, although the studies use similar inversion techniques that employ Mogi source modeling (Mogi, 1958). For example, Calais et al. (2008) proposed two Mogi sources for the initial 2007 events, one beneath Gelai (3 km depth, 0.01 $km^3$) and one between Ol Doinyo Lengai and Gelai (10 km depth, 0.05 $km^3$); however; Biggs et al. (2009) proposed one Mogi source beneath Gelai between 4 and 8 km depth and a total volume change of 0.4 $km^3$. The tectono-magmatic events continued into 2008 with another 3.8 m long dike intrusion near Ol Doinyo Lengai at a depth of 3.4 km and the deflation of a shallow 3 km deep magma reservoir beneath Ol Doinyo Lengai (Biggs et al., 2013).

More recent seismic studies reveal a complex network of magma storage from magma sources, through the crust, and upward to the surface. For example, Roecker et al. (2017) used a tomographic inversion to locate a magma reservoir in the lower crust-upper mantle that is responsible for supplying magma to a single reservoir seated in the mid-crust at 15 km depth beneath and between the two volcanoes. They proposed that the mid-crustal magma reservoir acts as the primary source of magma for Ol Doinyo Lengai. Reiss et al. (2021) presented shallow seismicity activity at a depth ranging from 3 to 10 km beneath Gelai while the deepest seismicity is observed at a depth of 20 km between Ol Doinyo Lengai and Gelai. These seismicity patterns were interpreted to correspond to a shallow and a deep-seated magma source in which the melt and volatiles are transported to the surface through dike intrusions and sills. Finally, tomographic mapping in 3D has shown a multitude of shallow cooled dike intrusions (< 6 km) linking to a silicate complex of intruded molten rock at 8–12 km deep facilitating fluid withdrawal from the two magma sources (Reiss et al., 2022).

In this work, we use satellite geodetic techniques (GNSS and InSAR) and non-linear inverse modeling to characterize the geodetically detectable aspects of the volcanic plumbing system toward a better assessment of volcano related hazards of Ol Doinyo Lengai.

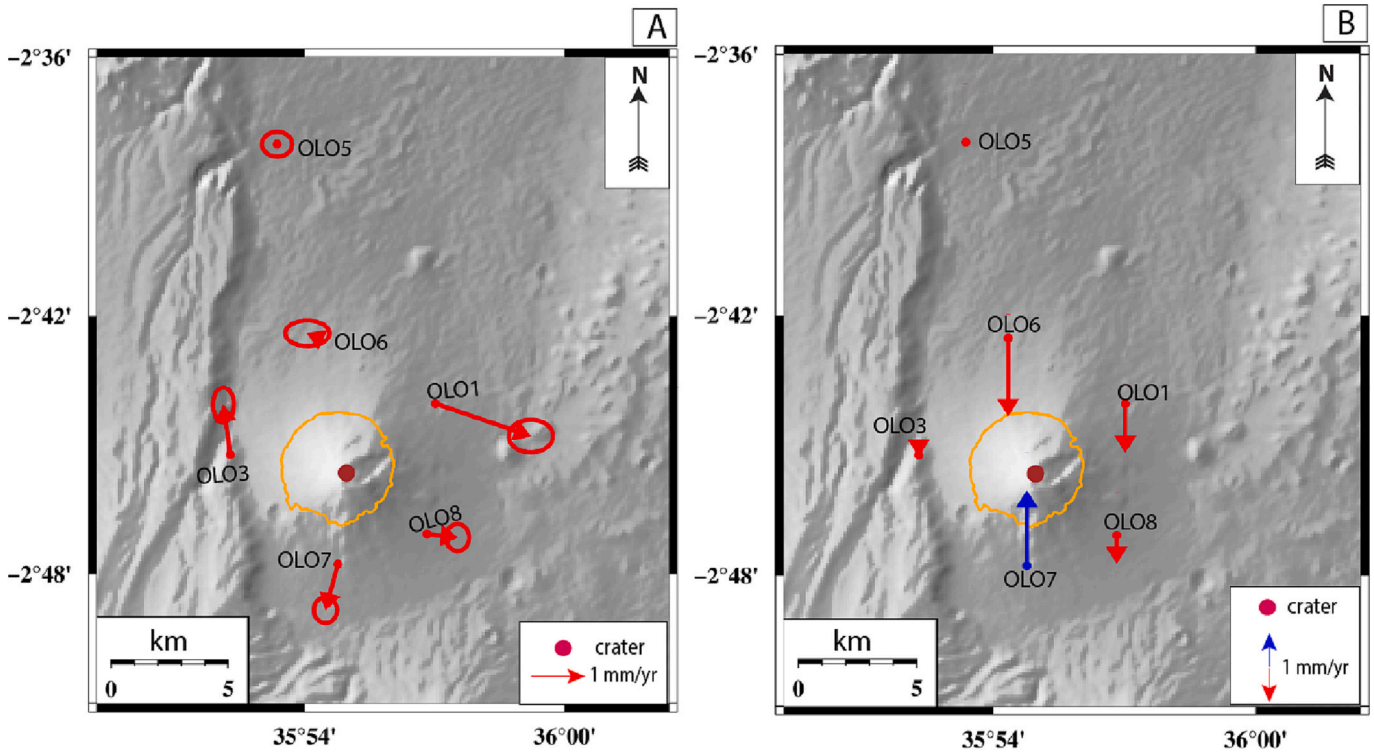


**Fig. 4.** GNSS velocity solutions. (A) TZVOLCANO horizontal velocity field solutions with respect to a fixed OLO5 with 95% uncertainties. (B) Vertical velocity field solutions relative to OLO5. The contour (orange line) is an outline of part of Ol Doinyo Lengai to aid with visualization. The filled red circle is the active volcanic crater. (For interpretation of the references to colour in this figure legend, the reader is referred to the web version of this article.)

## 3. Methods

The input data in this study are continuous Global Navigation Satellite System (GNSS) measurements from the TZVOLCANO network and Interferometric Synthetic Aperture Radar (InSAR) observations. The reason for using both datasets come from their capability to measure displacements on Earth's surface with different spatial and temporal resolution. GNSS provides daily three-dimensional observations with millimeter precision, but sparse spatial coverage, while InSAR provides better spatial coverage, but with less precision, only two dimensions (east-west and vertical) and less frequency of observations. Given the sparse distribution of GNSS instrumentation around the remote volcano, InSAR data are used to complement these measurements. The GNSS data are open access (Stamps et al., 2016a, 2016c, 2016e; Stamps et al., 2017a-c) and have been downloaded from the UNAVCO archive. The Sentinel-1 InSAR data are open access (Copernicus Sentinel data, 2021) and freely available in the Alaska Satellite Facility.

### 3.1. Global Navigation Satellite System (GNSS) observations

We use approximately 5 years of GNSS data (2016–2021) from the TZVOLCANO network. We process the five years of daily GNSS observations using the GAMIT-GLOBK software (Herring et al., 2018) following the procedures described in Reilinger et al. (2006), Calais et al. (2006), Stamps et al. (2008), and Saria et al. (2013). We process GNSS phase observables using double differencing to obtain the final position time-series and velocity solutions with their uncertainties. We estimate the satellite state vectors, tropospheric zenith delay parameters per site and per day, phase ambiguities using IGS final orbits and Earth orientation parameters. Also, our processing approach applies absolute antenna phase center models, solid Earth and polar tide corrections, and ocean loading corrections with the eight principal diurnal and semi-diurnal tidal constituents.

The results are a loose position solution for each day with their corresponding variance-covariance matrix combined with a global solution to estimate daily position time-series that were evaluated for outliers, offsets, and discontinuities. After cleaning the daily solutions, we performed a GLOBK forward run to compute the final velocity solution. We carefully evaluate the velocity uncertainties to ensure they are not overestimated or underestimated through the final covariance matrix. Here, the requirement is that the final prefit-chi square per degrees of freedom ($x^2$) should be near 1 (Floyd and Herring, 2020). Our final chi2 $x^2$ is 1.05. The resulting solution comprises the position and velocity of each processed GNSS site with the corresponding covariance matrices (Table 1). The residual time-series from the TZVOLCANO network with the mean secular signal removed are shown in Fig. 3. We evaluate the time-correlated noise characteristics of the velocity solution using the real-sigma algorithm implemented in GAMIT/GLOBK (Reilinger et al., 2006). In addition, we account for white noise, flicker noise, and annual and semi-annual signals that are likely to affect the solutions using the code HECTOR (Bos et al., 2013). However, OLO7 was processed simply using a linear model because the noise modeling and corrections are only appropriate for datasets with 2.5 years in length or longer (Blewitt and Lavallée, 2002). The resulting velocity field (Fig. 4) is used in the inversion of ground deformation around Ol Doinyo Lengai.

To filter the volcanic deformation from the tectonic motion, we defined a local reference frame by fixing one single GNSS site, OLO5 (see Herring et al., 2018, p. 47). We use OLO5 as a local reference station because it is outside the influence of volcanic activity since it is located 19 km north of the volcano (see Fig. 2). Also, the time-series for OLO5 (Fig. 3C) do not show significant deviation from a mean and therefore indicate it is stable which indicates OLO5 is a reasonable local reference station. In Table 1, we present GNSS velocity solutions relative to OLO5 (Fig. 4A, Fig. 4B), as well as the InSAR velocity solution for approximately the same timeframe of June 2016 to July 2021, relative to OLO5 as well (Table 1; Fig. 7).

The two GNSS sites with the largest horizontal deformation velocities are OLO1 and OLO7. OLO1 has a maximum horizontal velocity

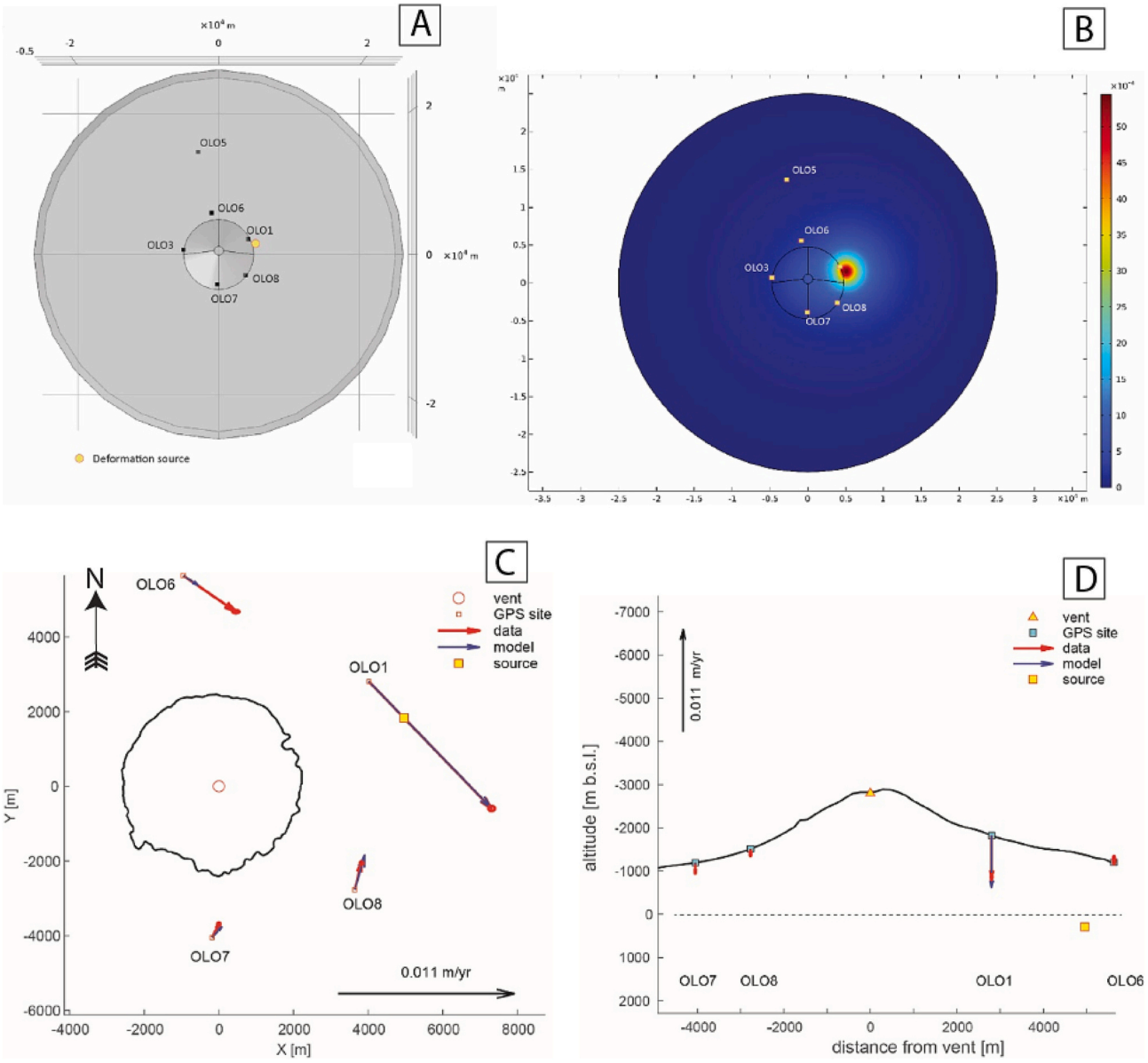


**Fig. 5.** Verification of the effectiveness of the TZVOLCANO GNSS network geometry (see Table 2 and Table 3). (A) Finite Element Model set up with the source shown as a yellow filled circle near OLO1. (B) Surface displacement magnitude of the Finite Element Model. The red colour is centered on the synthetic magma reservoir. (C) Results of the synthetic test for the horizontal components. Input velocities from the Finite Element Model are red vectors located at each of our GNSS station locations. Blue vectors are the results of the inversion. The yellow square is the location of the magma reservoir. (D) Same as (C) but for the vertical components. Topography is along a S—N profile along the zero axis shown in (C) with the vertical displacements from each station projected onto the profile. (For interpretation of the references to colour in this figure legend, the reader is referred to the web version of this article.)

**Table 2**
The synthetic dataset employed to verify the effectiveness of the TZVOLCANO GNSS network geometry. The relative positions of the GNSS sites, and the uncertainties of the deformation velocities are the same of TZVOLCANO (see Table 1 for the uncertainties). We add 20% of white Gaussian noise to the synthetic dataset with a Signal-to-Noise-Ratio = 5. "noisy" refers to the synthetic dataset with the additional Gaussian noise added.

| Site | X [m] | Y [m] | E [m/yr] | | N [m/yr] | | U [m/yr] | |
|---|---|---|---|---|---|---|---|---|
| | | | | noisy | | noisy | | noisy |
| OLO1 | 4014 | 2085 | 0.0103 | 0.0147 | −0.0137 | −0.0152 | −0.0184 | −0.0172 |
| OLO6 | −954 | 5638 | 0.0021 | 0.0063 | −0.0010 | −0.0043 | −0.0005 | 0.0009 |
| OLO7 | −182 | −4051 | 0.0023 | 0.0008 | 0.0018 | 0.0016 | −0.0003 | −0.0039 |
| OLO8 | 3640 | −2775 | 0.0025 | 0.0008 | 0.0049 | 0.0032 | −0.0024 | −0.0018 |

magnitude of 2.2 ± 0.2 mm/yr SE, relative to OLO5 and is subsiding at −5.7 ± 1.0 mm/yr (Table 1). OLO7 is moving in SW at a magnitude of 1.4 ± 0.3 mm/yr, relative to OLO5. All sites, except OLO7, show subsidence patterns with a maximum subsidence velocity at OLO6 of −3.3 ± 1.7 mm/yr. We suspect that the uplift at OLO7 is due to the short time span of the observations. The corresponding InSAR velocity

**Table 3**
Comparison between the parameters of the FEM model and the best-fit parameters recovered by the inversion with dMODELS of datasets mimicking the GNSS. Errors are 2-sigma. FEM and analytical models are available for download via Zenodo (Daud et al., 2023).

| Model | $X_0$[m] | $Y_0$ [m] | Depth [m b.s.l.] | Volume change [$10^6$ $m^3$] |
|---|---|---|---|---|
| Synthetic (FEM) | 5000 | 1500 | 500 | −0.60 |
| GNSS SNR = 5 | 4960 ± 160 | 1829 ± 204 | 293 ± 300 | −0.48 ± 0.14 |

solutions relative to the local reference site OLO5 (Table 1) shows a comparable pattern. For example, the GNSS easting velocity for OLO3 and OLO6 is positive as for their counterpart InSAR velocity. All InSAR vertical velocities show subsidence consistent with GNSS vertical motions except at OLO7.

To verify the effectiveness of the TZVOLCANO GNSS network geometry in constraining an offset shallow spherical magma source, we develop a Finite Element Model that mimics the topography of Ol Doinyo Lengai and has an offset deflating spherical source (250 m radius) at a depth of 500 m b.s.l (Fig. 5A). The dimensionless pressure change is defined as 0.0015, which equates to a volume change of $-0.6 \times 10^6$ $m^3$. We produce a synthetic surface velocity dataset (Fig. 5B) and extract velocities at each of our GNSS station locations used in our inversions (OLO1, OLO6, OLO7, OLO8; Fig. 5C,D). We add 20% of white Gaussian noise to the synthetic dataset with a Signal-to-Noise Ratio (SNR) of 5 to produce a "noisy" velocity solution (Table 2) and use the uncertainties from our GNSS velocity solution as the uncertainties for the inversion.

We invert the synthetic velocities for a spherical source with topographic corrections using dMODELS (see section 3.3 for details) with the results shown in Fig. 5C and D. The inversion of the noisy synthetic dataset (synthetic data plus white Gaussian noise) at the 4 stations can resolve the 4 parameters of the spherical source (surface location, depth, and volume change) within 2-sigma uncertainties (Table 3).

### 3.2. Interferometric Synthetic Aperture Radar (InSAR) data

We use five years of the Copernicus Sentinel-1 Synthetic Aperture Radar (SAR) C-band (wavelength ~ 56 mm) data (Copernicus Sentinel data, 2021), from June 2016 to July 2021, to generate Interferometric Synthetic Aperture Radar (InSAR) images. This time interval covers approximately the same time span of the GNSS observations. We process the SAR data using the Scientific Computing Environment (ISCE) TOPS stack processor (Rosen et al., 2012; Fattahi et al., 2017). We use the Miami INsar Time-series software (MintPy; Yunjun et al., 2019) to generate the InSAR time-series. We include in our analysis all the Sentinel-1 SAR acquisitions (single-look complex) available in tracks 130 and 152. Between June 2016 and July 2021, there are 159 scenes available for track 159 and 89 scenes for track 152. We set the maximum acquisition network span between interferograms as 3 adjacent scenes in the ISCE stack processor.

The time-series processing is mainly done using MintPy, with a temporal coherence threshold of 0.3 and mask threshold for a network inversion process of 0.1. We use a weather model for troposphere noise correction. The weather model was downloaded from the European Centre for Medium-Range Weather Forecasts (ECMWF) Reanalysis fifth Generation weather model products (Hersbach et al., 2020).

The time-series for Line-of-Site (LOS) displacements of two points far from the volcano relative to OLO5 (Fig. 6) illustrate how we assess the noise of the InSAR data. Fig. 6A is for a point in the far NE of the model domain, while Fig. 6B is for a point in the far SE of the model domain. The error bar of each point in the top panels is an indication of the noise level of each SAR acquisition, based on estimating the standard deviation of a reference region that is not considered tectonically or volcanically active. The scattered distribution of InSAR samples in both ascending and descending tracks indicate the noise structure between acquisitions. We find roughly 1 cm of scattering in the time-series (see bottom panels of Fig. 6).

From the InSAR time-series for both ascending (track 130) and descending (track 152) tracks, we can estimate the mean east-west and vertical surface velocities (Fig. 7) using the equations described in Huang and Evans (2019). We neglect the contribution of north-south velocities because InSAR is not sensitive to north-south motions. To adjust InSAR velocities for the same reference framework of GNSS, we define a stable reference for InSAR deformation and time-series from the mean velocity of InSAR pixels within 0.09 $km^2$ from OLO5. We compare the mean LOS velocities for ascending and descending InSAR with the GNSS equivalent in Fig. 7A-D. The descending and vertical mean velocities (Fig. 7B,D) show a linear subsidence northeast of the crater.

We compare the GNSS and InSAR vertical and horizontal components of deformation velocities in Fig. 8, and their time-series for horizontal and vertical motions in Fig. 9. The linear correlation between the deformation velocities indicates a reasonable agreement between the

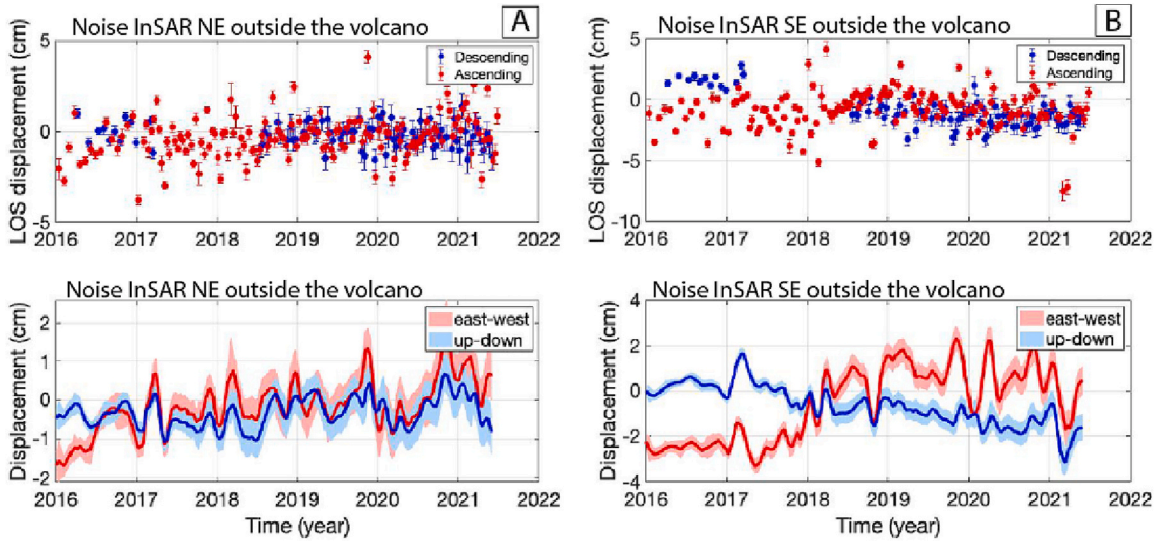


**Fig. 6.** Time-series of InSAR data for two areas located NE (A) and SE (B) of Ol Doinyo Lengai far from volcanic activity. The time-series are relative to OLO5. Top figures show LOS displacements. Bottom figures show the scattering of east-west and up-down displacements.

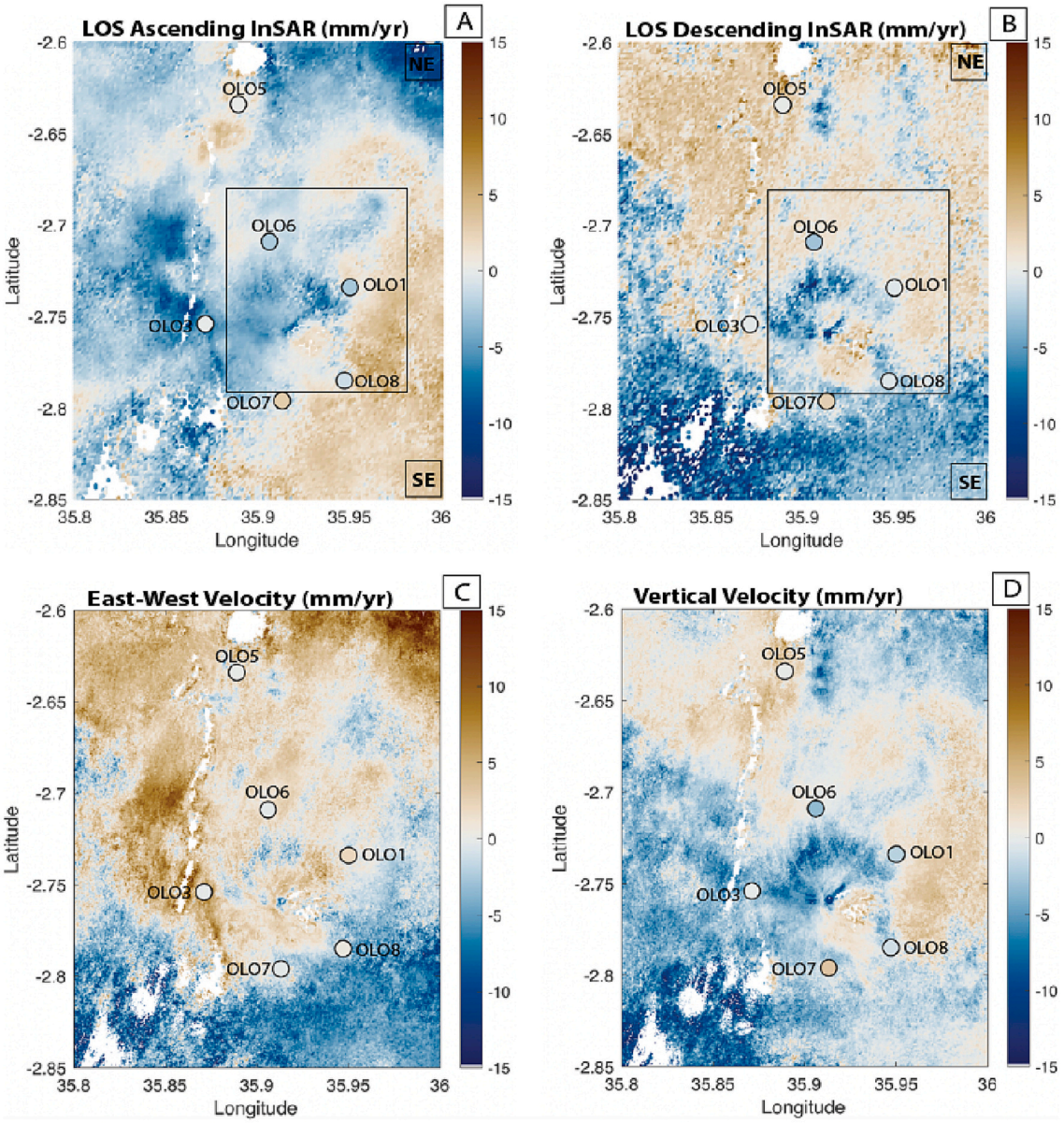


**Fig. 7.** Mean LOS velocities for ascending (A) and descending (B) InSAR overlain with the GNSS equivalent. The colored circles represent GNSS mean velocity projected to ascending line-of-sight. Positive values indicate moving toward the satellite. B. InSAR descending mean velocity adjusted to the GNSS reference frame. The colored circles represent GNSS mean velocity projected to ascending line-of-sight. Positive values indicate moving toward the satellite. The black boxes in A and B indicate the region shown in Figs. 11 and 12. C. Mean velocity in east-west component (positive means eastward) based on InSAR. D. Vertical mean velocity (positive means uplift) based on InSAR. The colored circles are the GNSS stations. There is a localized linear subsidence feature northeast of the crater that is not observed in the east-west component.

two datasets.

### 3.3. Numerical modeling

We use dMODELS, an open-source software package by the US Geological Survey (Battaglia et al., 2013a, 2013b) to model the deformation. The software dMODELS, can invert GNSS and InSAR data separately, or jointly. The software is designed for the MATLAB environment with functions to invert geodetic data using analytical kinematic models. The crust is described as a homogeneous, isotropic, linearly elastic half-space. Its inversion algorithm for hyper-parameter optimization combines randomly chosen trials with an interior-point, non-linear optimization algorithm (Bergstra and Bengio, 2012). The cost function of the optimization algorithm is the weighted chi-square per degrees of freedom ($\chi^2_\nu$). The assumption of linear elasticity is appropriate for the region of Ol Doinyo Lengai because the deformation is small compared to dimension of the volcano (see Dvorak and Dzurisin, 1997), and there is insufficient information to constrain a more complex rheology.

We invert GNSS and InSAR observations (both separately and jointly, see Table 4 and Table 5) to estimate the parameters of a finite spherical magma source. The algorithm is based on the spherical model by McTigue (1987) with the topographical correction by Williams and Wadge (1998). The model parameter uncertainties are computed following the algorithm described in Wright et al. (1999). Inverting for an expanding, or contracting, finite spherical source (McTigue, 1987) results in four resolved parameters: the volume change, surface location ($X_0$, $Y_0$), and depth. The modules of dMODELS employed in this paper are available for download on Zenodo (Daud et al., 2023).

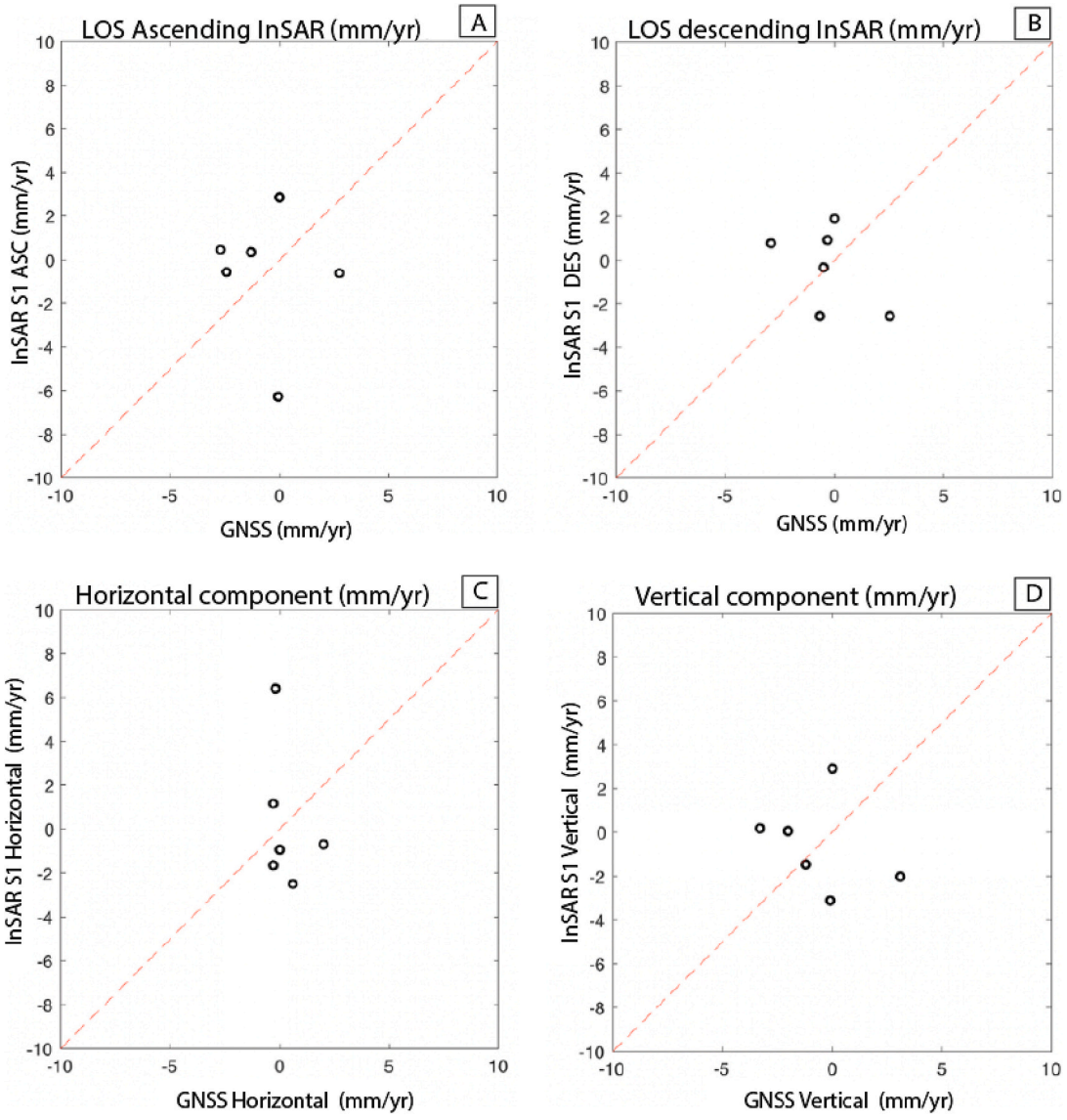


**Fig. 8.** Comparison between InSAR and GNSS mean velocities. (A) and (B) GNSS velocities are projected along the Line-of-Site (LOS) of the satellite. (C) and (D) InSAR LOS velocities are decomposed in the horizontal and vertical components.

## 4. Results

### 4.1. Inverse modeling of GNSS velocities with dMODELS

We present in Table 4, the best-fit result (model parameters and their respective 1 standard deviation uncertainties) of our inversion of GNSS deformation velocities. We used four GNSS stations (OLO1, OLO6, OLO7, and OLO8) in the inversion. The GNSS station OLO3 was excluded because of its location close to the Natron Fault. This site is used to constrain the behavior and motion of the Natron Fault, which is not a focus of this study. The best-fit source is a shallow spherical source, NE of the volcano near OLO1 (Fig. 10). The depth is 3408 ± 29 m beneath the summit (vent) of Ol Doinyo Lengai (altitude of summit ~2908 m a.s.l.) corresponds to ~500 m below sea level.

The software dMODELS, does not invert for the radius of a spherical source because of the trade-off between radius and pressure change (McTigue, 1987) for horizontal and vertical deformation, therefore we tested a range of source radii (200–600 m). A radius of 500 m provides the best-fit model with respect to the penalty function and depth of the source. To verify the consistency of the inversion results, we varied the number of random grid searches from 64 to 512 to confirm a consistent location and depth of the shallow spherical source. Finally, we compute the model parameters and uncertainties of our best-fit source (Table 4) using the Monte-Carlo approach proposed by Wright et al. (1999).

Our GNSS inversion results infer a small, deflating, shallow deformation source located NE between Ol Doinyo Lengai and the dormant Gelai volcano consistent with the depth of a magma reservoir that feeds Ol Doinyo Lengai determined by a petrological study by Petibon et al. (1998). We provide the best-fit solutions for the GNSS inversion as well as all model input and output files necessary to reproduce the results in a Zenodo repository (Daud et al., 2023). In Table 5, we list the parameters from the GNSS inversion, the InSAR inversion, and the joint inversion.

### 4.2. Inverse modeling of InSAR data with dMODELS

We invert the ascending and descending InSAR data sub-sampled by 50% for a spherical source to be consistent with the GNSS inversions. Initially we tried to invert all of the available InSAR data, but do not find convergence. Then we selected smaller and smaller sub-domains until we found convergence. The region shown in Fig. 11 is the sub-domain shown as a black box in Fig. 7A,B that ultimately converged. A shallow, deflating spherical source converges to a stable solution with a

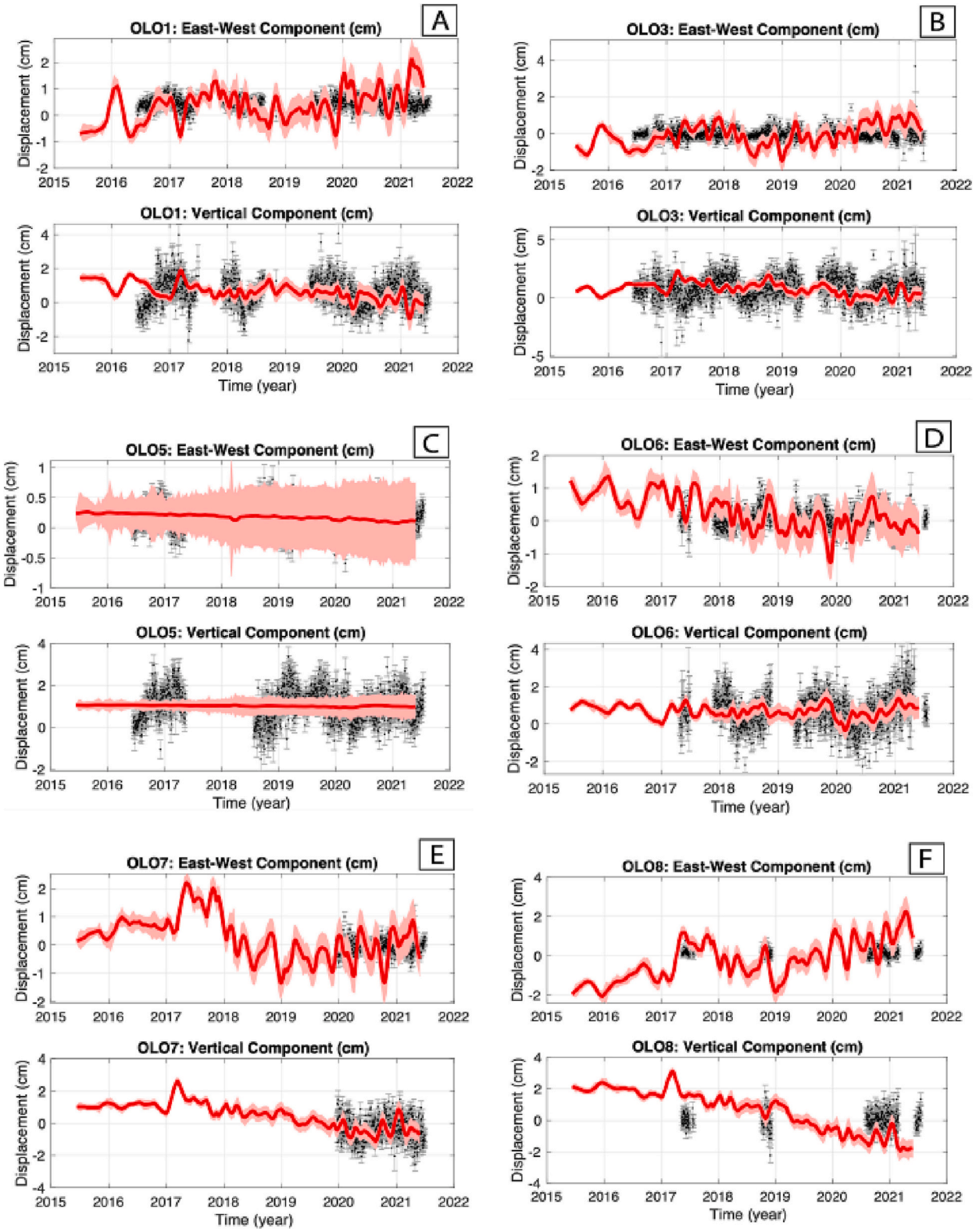


**Fig. 9.** InSAR (red) and GNSS (black) time-series from 2016 to 2021. East-west and up-down components at the locations of (A) OLO1, (B) OLO3, (C) OLO5 (D) OLO6, (E) OLO7, and (F) OLO8 GNSS sites. Line-of-Sight displacement is referenced to pixels close to the stable site OLO5. (For interpretation of the references to colour in this figure legend, the reader is referred to the web version of this article.)

500 m radius and a volume change of $-0.39 \pm 0.33 \times 10^6\ m^3$ in a similar location as constrained by the GNSS data (Table 4). Uncertainties are computed using the same approach of the GNSS inversion (Wright et al., 1999). Fig. 11 shows the data, model, and misfit in ascending and descending orbits for the InSAR inversion. We provide the best-fit solutions as well as all model files necessary to reproduce the results in the Zenodo repository of Daud et al. (2023).

**Table 4**
Modeling results from the inversion of GNSS velocities using a finite spherical source (McTigue, 1987) with a topography correction and a radius of 500 m. $X_0$, $Y_0$: location of deformation source, relative to Ol Doinyo Lengai. Uncertainties are 1 standard deviation.

| Random searches | $\chi^2_\nu$ | $X_0$ (m) | $Y_0$(m) | Depth (m b.s.l) | Volume change ($10^6$ m$^3$) |
|---|---|---|---|---|---|
| 256 | 8.4 | 5309 ± 1497 | 2368 ± 2510 | 500 ± 29 | −0.04 ± 0.05 |

Data and model velocity at each station. 1-sigma uncertainties are provided.

| Site | X | Y | alt | $V_E$ | $V_E$ Model | $\sigma_E$ | $V_N$ | $V_N$ Model | $\sigma_N$ | $V_U$ | $V_U$ Model | $\sigma_U$ |
|---|---|---|---|---|---|---|---|---|---|---|---|---|
| | M | m | m | mm/yr | mm/yr | mm/yr | mm/yr | mm/yr | mm/yr | mm/yr | mm/yr | mm/yr |
| OLO1 | 4014 | 2805 | 988 | 2.0 | 1.7 | 0.4 | −0.7 | −0.6 | 0.3 | −2.0 | −1.9 | 1.2 |
| OLO6 | −954 | 5638 | 908 | −0.3 | 0.2 | 0.4 | 0.1 | −0.1 | 0.3 | −3.3 | −0.0 | 1.4 |
| OLO7 | −182 | −4051 | 1449 | −0.3 | 0.1 | 0.2 | −1.0 | 0.1 | 0.2 | 3.1 | −0.0 | 0.7 |
| OLO8 | 3640 | −2775 | 1237 | 0.6 | 0.1 | 0.2 | −0.1 | 0.3 | 0.2 | −1.2 | −0.1 | 1.2 |

**Table 5**
Best-fit parameters for a spherical source from the GNSS, InSAR, and joint inversions with 1 standard deviation uncertainties provided. The relative weights for the joint inversion were $w_1$ (InSAR) = 0.25 and $w_2$ (GNSS) = 0.75. This choice gave approximately equal values of the RMSE for GNSS and InSAR.

| Dataset | $X_0$ [m] | $Y_0$ [m] | Depth [m b.s.l.] | Volume change [$10^6$ m$^3$] |
|---|---|---|---|---|
| GNSS | 5309 ± 1497 | 2368 ± 2510 | 500 ± 29 | −0.04 ± 0.05 |
| InSAR | 2050 ± 229 | 1816 ± 194 | 3606 ± 770 | −0.39 ± 0.29 |
| GNSS + InSAR | 4998 ± 612 | 2440 ± 256 | 501 ± 57 | −0.04 ± 0.01 |

### 4.3. Joint inversion of GNSS and InSAR data

Finally, we run a joint inversion of the GNSS and InSAR data (both ascending and descending components) for a spherical source. The cost function in the inversion algorithm is the weighted sum of the normalized root mean square error (*RMSE*) of InSAR and GNSS data (Toraldo Serra et al., 2013):

$$RMS = \sum_{j=1}^{2} w_j \left[ \sqrt{\frac{\sum_{i=1}^{n} (d_i - m_i)^2}{\sum_{i=1}^{n} d_i^2}} \right]_j \frac{j = 1\ InSAR}{j = 2\ GNSS} \quad (1)$$

where $d_i$ are the data, $m_i$ the model results, and $w_j$ the relative weights. Uncertainties are calculated using the same Wright et al. (1999) approach also used for the GNSS and InSAR inversions. In the application presented in this study, we chose to weight the GNSS datasets three times more than InSAR ($w_1$ = 0.25 and $w_2$ = 0.75). This choice gave approximately equal values of the *RMSE* for GNSS and InSAR. The results from the joint inversion suggest a shallow, deflating source in approximately the same location as the independent inversions within 2-sigma uncertainties. Fig. 12 shows the spherical source from joint inversion, and Table 5 compares the results from the GNSS, InSAR, and joint inversions with uncertainties. All model input and output files are provided in the Zenodo repository of Daud et al. (2023).

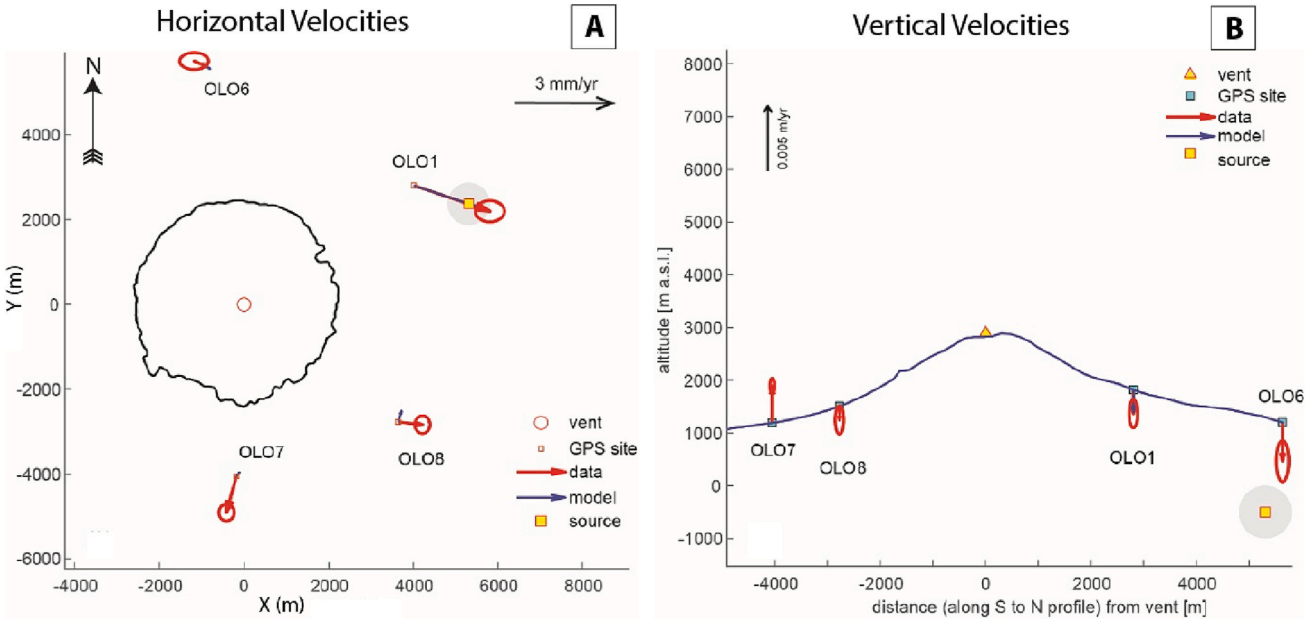


**Fig. 10.** Best-fit model for the GNSS deformation velocities (see Table 4). Horizontal (A) and vertical (B) velocities: model results (blue), GNSS velocities (red). The contour in (A) is the outline of Ol Doinyo Lengai at 1750 m a.s.l. The elevation profile in (B) is along a S—N profile from OLO7 to OLO6. The gray circle shows the size of the spherical source (radius 500 m). Volcanic crater is a red circle (A) or yellow triangle (B). (For interpretation of the references to colour in this figure legend, the reader is referred to the web version of this article.)

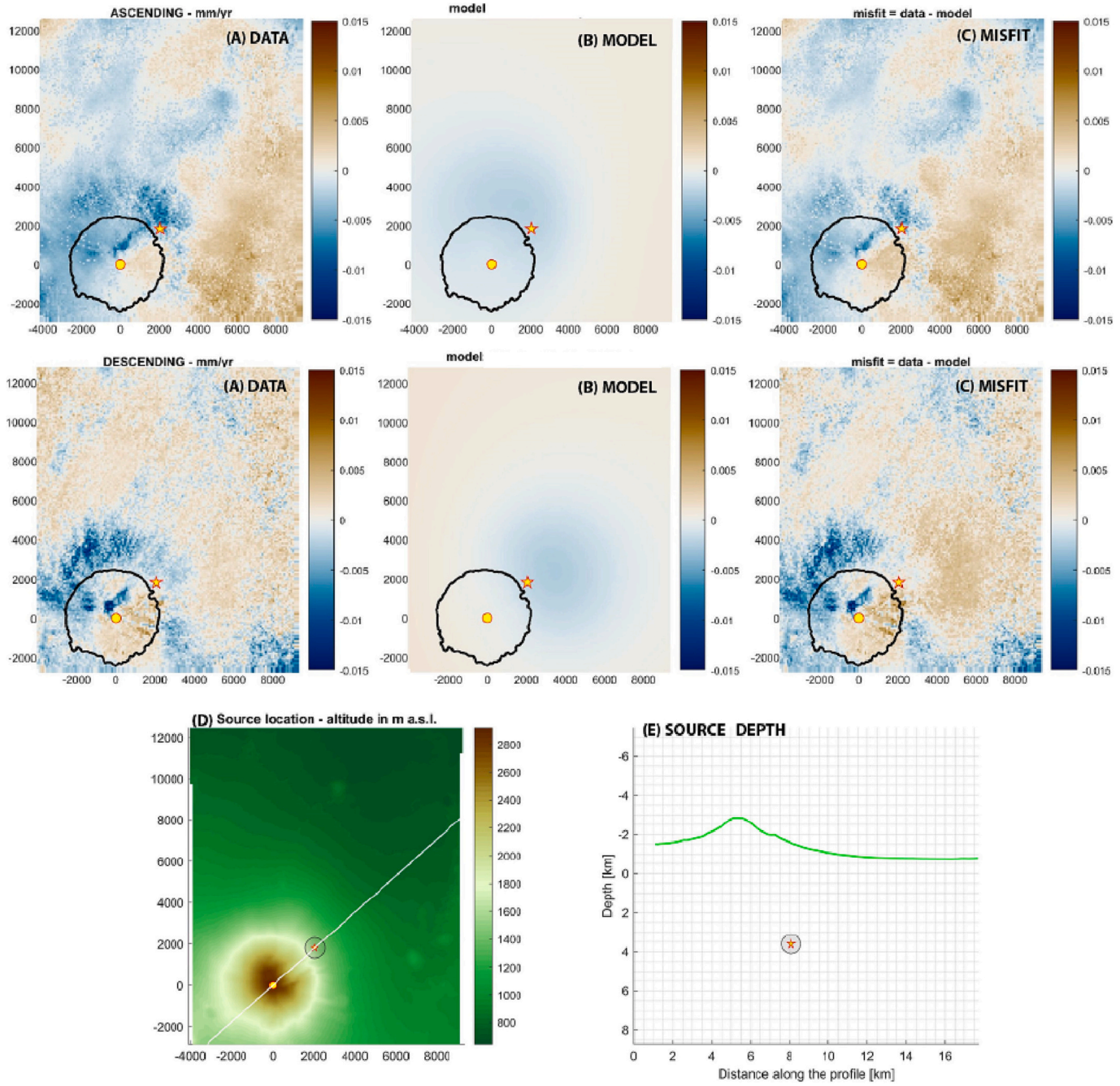


**Fig. 11.** Best-fit solution for a spherical source from the inversion of InSAR deformation from June 2016 to July 2021. Ascending (or descending) orbit: (A) InSAR data line-of-sight velocities; (B) best-fit model; (C) residuals; pixels where the residual is smaller than 1-σ are white. The crater is a circle in yellow and the source location is a star in yellow. The white and black contours are the outline of Ol Doinyo Lengai at 1750 m a.s.l. (D) Source location plotted over the DEM of Ol Doinyo Lengai. (E) Source depth; the green line is the topography along the white profile in (D). (For interpretation of the references to colour in this figure legend, the reader is referred to the web version of this article.)

## 5. Discussion

Both GNSS and InSAR measurements depict subsidence at a low rate (−1 to −6 mm/yr). Although our numerical modeling results are non-unique and our data have small signals, the consistent inversion results from GNSS, InSAR, and the joint inversion suggest an offset shallow deflating magma source (~3.5 km beneath the elevation of the volcano summit), detectable with our geodetic observations. Furthermore, the source parameters from the independent inversions and the joint inversion are consistent within 2-sigma errors (Fig. 10, Fig. 11, Fig. 12; Table 5). This proposed magma source is located between Ol Doinyo Lengai and the dormant Gelai at a depth supported by petrological analysis (Petibon et al., 1998). The location is above the sill complex detected by Reiss et al. (2022), above the reservoir proposed by Calais et al. (2008) at 10 km depth between Ol Doinyo Lengai and Gelai, and east of the two magma sources beneath Gelai resolved by Calais et al. (2008) and Biggs et al. (2009). Biggs et al. (2013) suggested the existence of another magma reservoir beneath Ol Doinyo Lengai at a similar depth, but our source is northeast of the formerly resolved magma reservoir in that study. Also, Roecker et al. (2017) and Reiss et al. (2021, 2022) suggested the existence of a deep magma reservoir using seismic observations (15–20 km). Additional support for a deeper magma

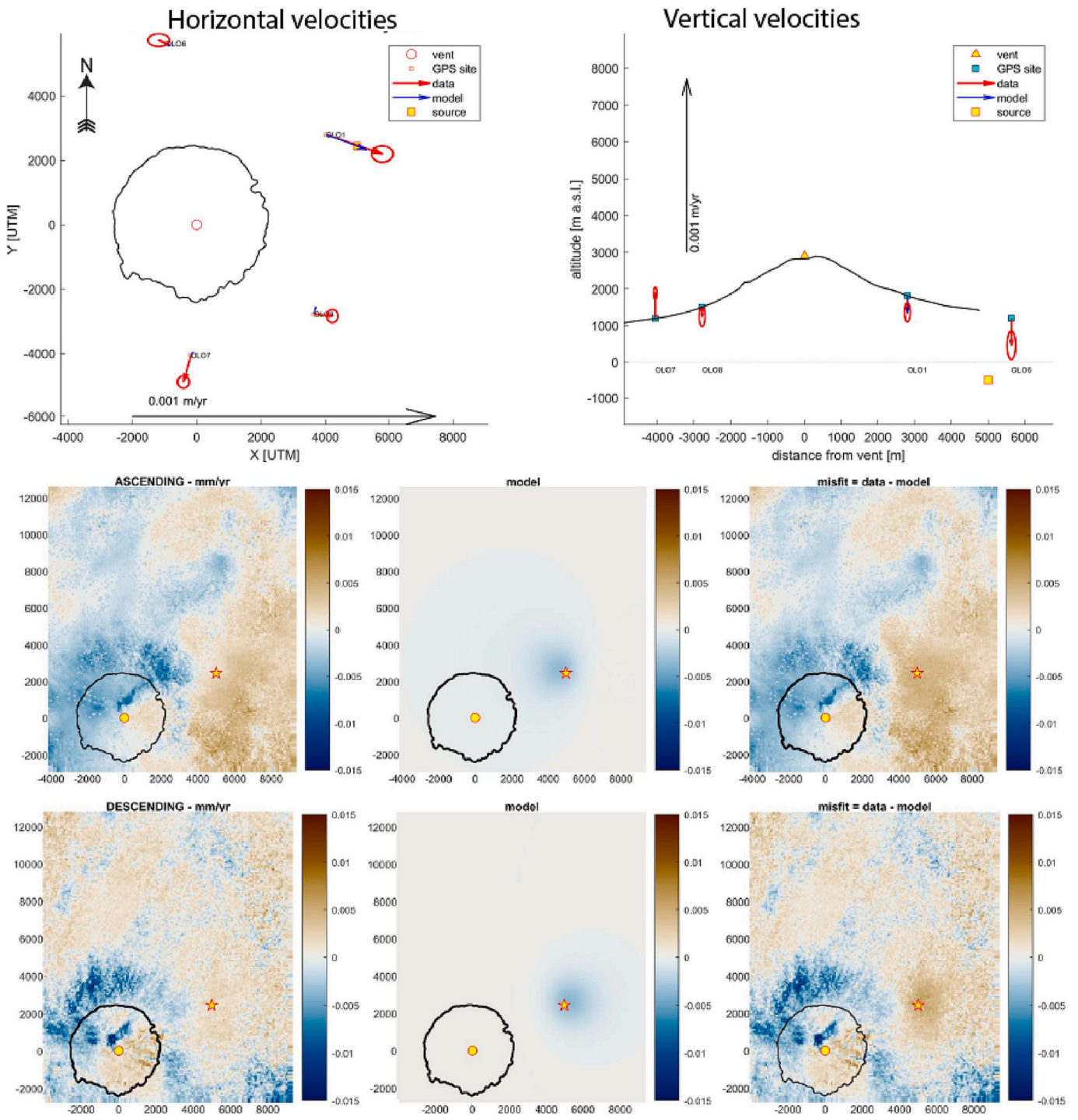


**Fig. 12.** Best-fit for the joint inversion of GNSS and InSAR displacements. (TOP) Horizontal and vertical GNSS velocities with the profile in right figure along a N-S line from OLO7 to OLO6 that crosses the volcanic vent; contour is the outline of Ol Doinyo Lengai at 1750 m a.s.l. The magma source is a yellow-filled square to the northeast of the volcano, near OLO1. Volcanic crater is a red circle or yellow triangle. (CENTER) Ascending orbit: (A) InSAR data line-of-sight velocities; (B) best-fit model; (C) residuals – pixels where the residual is smaller than 1-σ are blank. (BOTTOM) Descending orbit: (A) InSAR data line-of-sight velocities; (B) best-fit model; (C) residuals; pixels where the residual is smaller than 1-σ are white. (For interpretation of the references to colour in this figure legend, the reader is referred to the web version of this article.)

reservoir comes from previous geodetic studies (Baer et al., 2008; Biggs et al., 2013). They proposed an undetected dike was sourced from a deeper magma reservoir that preceded the initial 2007 Gelai Fault slip. Further, stress computations and estimates of magma volumes from petrological measurements suggest that a single shallow magmatic source could not be enough for the 2007–2008 eruptions (Kervyn et al., 2010; Biggs et al., 2013). Given the small volume change found in this study (~0.04 × $10^6$ $m^3$ for the GNSS and joint inversions), we suggest that the reservoir inferred from our measurements could be fed by this deeper reservoir (Fig. 13).

## 6. Summary and conclusions

Ol Doinyo Lengai is a little known volcano in the Natron Rift

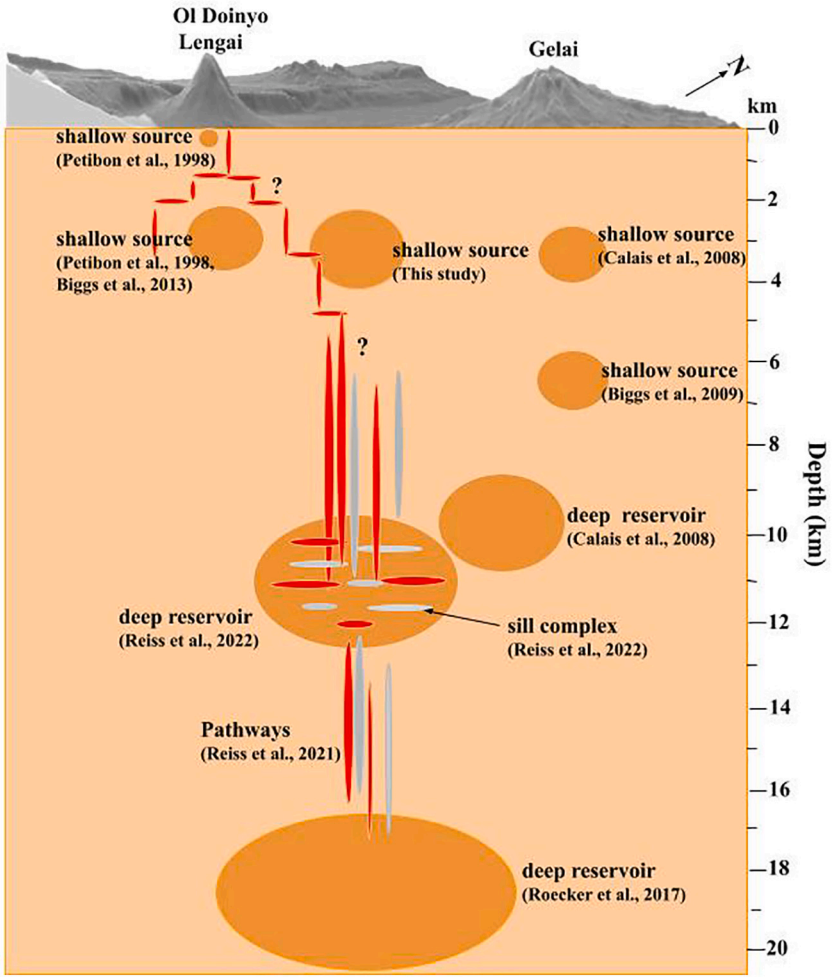


**Fig. 13.** A conceptual model geometry of the magma plumbing system of Ol Doinyo Lengai based on this work and previous studies (Petibon et al., 1998; Calais et al., 2008; Biggs et al., 2009, 2013; Roecker et al., 2017; Reiss et al., 2021, 2022).

(Tanzania; Fig. 1). Its remote location and the lack of accessible roads make studying and monitoring Ol Doinyo Lengai difficult. Despite numerous political and logistical challenges, since 2016, the TZVOLCANO GNSS network (Fig. 2) is monitoring surface deformation at Ol Doinyo Lengai and fault slip on the adjacent Natron Fault (Fig. 4**)**.

Modeling of data from the remote TZVOLCANO GNSS network and InSAR reinforce the conceptual model that Ol Doinyo Lengai is part of a fractured rift where magmatic fluids percolate to the surface from a deep reservoir (Fig. 13). We calculate the surface displacements from 6 permanent GNSS stations of the TZVOLCANO network, as well as from InSAR interferograms covering approximately the same time period (2016–2021) as the GNSS data. Although these datasets have small magnitude signals and the GNSS data are sparse, they are highly valuable for assessing the region for volcanic hazards. Both GNSS and InSAR data indicate subsidence around Ol Doinyo Lengai with similar magnitude. Independent and joint inversions of GNSS and InSAR data both indicate a shallow deflating volcanic source between the Ol Doinyo Lengai and Gelai volcanoes. This shallow source located east of Ol Doinyo Lengai and southwest of the dormant volcano Gelai is likely connected to a deep magma reservoir (Fig. 13).

This work, although based on imperfect data, suggests an offset multiple magma reservoir system exists in the Natron Rift with a shallow magmatic source east of the active Ol Doinyo Lengai volcano. It is worth noting that magma reservoirs are often significantly laterally offset from overlying volcanoes (Lerner et al., 2020). A network of fractures may exist that connects the shallow reservoir to the active crater. The offset magmatic system may control the stage, style, occurrences, and the magnitude of eruptive activity at the volcanic edifice of Ol Doinyo Lengai.

## Acknowledgments and data availability

This material is based on services provided by the GAGE Facility, operated by UNAVCO, Inc., with support from the National Science Foundation, the National Aeronautics and Space Administration, and the U.S. Geological Survey under NSF Cooperative Agreement EAR-1724794. We acknowledge and thank Alaska Satellite Facility for making InSAR data freely available (Copernicus Sentinel data, 2021) and TZVOLCANO GNSS datasets available through the UNAVCO data archive (Stamps et al., 2016a, 2016c, 2016e; Stamps et al., 2017a-c). Instrumentation and technical support were provided by UNAVCO. We highly appreciate Virginia Tech, KIGAM, Ardhi University for their initiation and establishment of the permanent GNSS monitoring network whose datasets have been largely used in this work. We also extend our gratitude to everyone involved in the fieldwork, including Kristofa Nkembo, Komiando Naibala Leiyan Laizer, the Community Based Organization (CBO) management's moral support, and the generosity from the members of Engaresero village. GAMIT-GLOBK software used in processing GNSS data is available at http://chandler.mit.edu/gg/ The USGS dMODELS code used to invert GNSS and InSAR surface deformation velocities can be accessed at through the Zenodo repository of Daud et al. (2023) or by contacting Maurizio Battaglia. All

model files necessary to reproduce the results can also be found at Daud et al. (2023) on Zenodo, and the software will be available through the USGS website code.usgs.gov/vsc/publications/OlDoinyoLengai or by contacting Maurizio Battaglia. We thank two anonymous reviewers for excellent constructive feedback that greatly improved this manuscript, particularly the amazing work done by anonymous reviewer 2. This work was funded by the National Science Foundation (NSF) grant number EAR-1943681 to Virginia Tech, the Basic Research Project (GP2021-006) to the Korea Institute of Geosciences and Mineral Resources (KIGAM) funded by the Ministry of science and ICT of Korea, and Ardhi University. Funding for this work also came from USAID via the Volcano Disaster Assistance Program and from the U.S. Geological Survey (USGS) Volcano Hazards Program. Any use of trade, firm, or product names is for descriptive purposes only and does not imply endorsement by the U.S. Government.

## CRediT authorship contribution statement

**Ntambila Daud:** Formal analysis, Investigation, Validation, Visualization, Writing – original draft. **D. Sarah Stamps:** Conceptualization, Formal analysis, Funding acquisition, Project administration, Validation, Supervision, Writing – review & editing, Resources. **Maurizio Battaglia:** Formal analysis, Methodology, Software, Writing – review & editing. **Mong-Han Huang:** Formal analysis, Methodology, Software, Writing – review & editing. **Elifuraha Saria:** Conceptualization, Funding acquisition, Project administration, Writing – review & editing, Resources, Project administration. **Kang-Hyeun Ji:** Conceptualization, Funding acquisition, Writing – review & editing, Resources.

## Declaration of Competing Interest

The authors declare that they have no known competing financial interests or personal relationships that could have appeared to influence the work reported in this paper.

## Data availability

I have archived the data at Zenodo and provided software links.

## References


Albaric, J., Perrot, J., Déverchére, J., Deschamps, A., Le Gall, B., Ferdinand, R.W., Petit, C., Tiberi, C., Sue, C., Songo, M., 2010. Contrasted seismogenic and rheological behaviors from shallow and deep earthquake sequences in the north Tanzanian divergence, East Africa. J. Afr. Earth Sci. 58 (5), 799–811. https://doi.org/10.1016/j.jafrearsci.2009.09.005.

Baer, G., Hamiel, Y., Shamir, G., Nof, R., 2008. Evolution of a magma driven earthquake swarm and triggering of the nearby Oldoinyo Lengai eruption, as resolved by InSAR, ground observations and elastic modeling, East African Rift. Earth Planet. Sci. Lett. 272, 339–352. https://doi.org/10.1016/j.epsl.2008.04.052.

Battaglia, M., Cervelli, P.F., Murray, J.R., 2013a. dMODELS: a MATLAB software package for modeling crustal deformation near active faults and volcanic centers. J. Volcanol. Geotherm. Res. 254, 1–4. https://doi.org/10.1016/j.jvolgeores.2012.12.018.

Battaglia, M., Cervelli, P.F., Murray, J.R., 2013b. Modeling crustal deformation near active faults and volcanic centers—a catalog of deformation models: U.S. In: Geological Survey Techniques and Methods, Book 13, chap. B1: 96. http://pubs.usgs.gov/tm/13/b1.

Battaglia, M., Alpala, J.A., Alpala, R.L., Angarita, M., Arcos, D., Euillades, L., Euillades, P., Muller, C., Medina, L.N., 2021a. Monitoring volcanic deformation. In: Alderton, D., Elias, S.A. (Eds.), Encyclopedia of Geology, , 2nd edition1. Academic Press, United Kingdom, pp. 774–804. https://doi.org/10.1016/B978-0-08-102908-4.00132-6.

Battaglia, M., Pagli, C., Meuti, S., 2021b. The 2008–2010 Subsidence of Dallol Volcano on the Spreading Erta Ale Ridge: InSAR Observations and Source Models. Remote Sens. 13 (10), 1991. https://doi.org/10.3390/rs13101991.

Bergstra, J., Bengio, Y., 2012. Random search for hyper-parameter optimization. J. Mach. Learn. Res. 13 (2).

Biggs, J., Amelung, F., Gourmelen, N., Dixon, T.H., Kim, S.W., 2009. InSAR observations of 2007 Tanzania rifting episode reveal mixed fault and dyke extension in an immature continental rift. Geophys. J. Int. 179 (1), 549–558. https://doi.org/10.1111/j.1365-246X.2009.04262.x.

Biggs, J., Chivers, M., Hutchinson, M.C., 2013. Surface deformation and stress interactions during the 2007–2010 sequence of earthquake, dyke intrusion and eruption in northern Tanzania. Geophys. J. Int. 195 (1), 16–26. https://doi.org/10.1093/gji/ggt226.

Blewitt, G., Lavallée, D., 2002. Effect of annual signals on geodetic velocity. Journal of Geophysical Research: Solid Earth 107 (B7), ETG–9. https://doi.org/10.1029/2001JB000570.

Bos, M.S., Fernandes, R.M.S., Williams, S.D.P., Bastos, L., 2013. Fast error analysis of continuous GNSS observations with missing data. J. Geod. 87 (4), 351–360. https://doi.org/10.1007/s00190-012-0605-0.

Burchardt, S., Galland, O., 2016. Studying volcanic plumbing systems–multidisciplinary approaches to a multifaceted problem. In: Updates in Volcanology-From Volcano Modelling to Volcano Geology: 23-53. https://doi.org/10.5772/63959.

Calais, E., Ebinger, C., Hartnady, C., Nocquet, J.M., 2006. Kinematics of the East African Rift from GPS and earthquake slip vector data. Geol. Soc. Lond., Spec. Publ. 259 (1), 9–22. https://doi.org/10.1144/GSL.SP.2006.259.01.03.

Calais, E., d'Oreye, N., Albaric, J., Deschamps, A., Delvaux, D., Déverchère, J., Wauthier, C., 2008. Strain accommodation by slow slip and dyking in a youthful continental rift, East Africa. Nature 456 (7223), 783–787. https://doi.org/10.1038/nature07478.

Cervelli, P.F., Fournier, T., Freymueller, J., Power, J.A., 2006. Ground deformation associated with the precursory unrest and early phases of the January 2006 eruption of Augustine Volcano, Alaska. Geophys. Res. Lett. 33, L18304. https://doi.org/10.1029/2006GL027219. Copernicus Sentinel data, 2021. Retrieved from ASF DAAC [1 September 2021], processed by ESA.

Copernicus Sentinel data, 2021. Retrieved from ASF DAAC [1 August 2021], processed by ESA.

Daud, Ntambila, Stamps, D. Sarah, Battaglia, Maurizio, Huang, Mong-Han, Saria, Elifuraha, Ji, Kang-Hyeun, 2023. Elucidating the Magma Plumbing System of Ol Doinyo Lengai (Natron Rift, Tanzania) Using Satellite Geodesy and Numerical Modeling: Supplementary Model Files (Version 4) [Data set]. Zenodo. https://doi.org/10.5281/zenodo.7897255.

Dvorak, J.J., Dzurisin, D., 1997. Volcano geodesy: the search for magma reservoirs and the formation of eruptive vents. Rev. Geophys. 35 (3), 343–384. https://doi.org/10.1029/97RG00070.

Dzurisin, D., 2006. Volcano Deformation: New Geodetic Monitoring Techniques. Springer Science and Business Media.

Fattahi, H., Agram, P., Simons, M., 2017. A Network-based Enhanced Spectral Diversity Approach for TOPS Time-Series Analysis. IEEE Trans. Geosci. Remote Sens. 55 (2), 777–786. https://doi.org/10.1109/tgrs.2016.2614925.

Fernandes, R.M.S., Delvaux, D., Miranda, J.M., Saria, E., Stamps, D.S., 2013. Re-evaluation of the kinematics of Victoria block using continuous GNSS data. Geophys. J. Int. 193, 1–10. https://doi.org/10.1093/gji/ggs071.

Floyd, M.A., Herring, T.A., 2020. Fast statistical approaches to geodetic time series analysis. In: Geodetic Time Series Analysis in Earth Sciences, 157-183. Springer, Cham. https://doi.org/10.1007/978-3-030-21718-1.

Hamling, I.J., Wright, T.J., Calais, E., Bennati, L., Lewi, E., 2010. Stress transfer between thirteen successive dyke intrusions in Ethiopia. Nature Geoscience 3 (10), 713–717. https://doi.org/10.1038/NGEO967.

Herring, T.A., King, R.W., Floyd, M.A., McClusky, S.C., 2018. Introduction to GAMIT/GLOBK, Release 10.7: GAMIT/GLOBK Documentation.

Hersbach, H., Bell, B., Berrisford, P., Hirahara, S., Horanyi, A., Munoz-Sabater, J., 2020. The ERA5 global reanalysis. Q. J. R. Meteorol. Soc. 146 (730), 1999–2049. https://doi.org/10.1002/qj.3803.

Huang, M.H., Evans, E.L., 2019. Total variation regularization of geodetically constrained block models in Southwest Taiwan. J. Geophys. Res. Solid Earth 124. https://doi.org/10.1029/2019JB018076.

Janssen, V., 2007. Volcano deformation monitoring using GPS. J. Spat. Sci. 52 (1), 41–54. https://doi.org/10.1080/14498596.2007.9635099.

Jerram, D.A., Bryan, S.E., 2015. Plumbing Systems of Shallow Level Intrusive Complexes. Advances in Volcanology. Springer International Publishing, Switzerland, pp. 1–22. https://doi.org/10.1007/978-3-319-14084-1.

Kervyn, M., Ernst, G.G.J., Keller, J., Vaughan, G., Klaudius, J., Pradal, E., Jacobs, P., 2010. Fundamental changes in the activity of the natrocarbonatite volcano Oldoinyo Lengai, Tanzania. II. Eruptive behavior. Bull. Volcanol. 72, 913–931. https://doi.org/10.1007/s00445-010-0360-0.

Lerner, A.H., O'Hara, D., Karlstrom, L., Ebmeier, S.K., Anderson, K.R., Hurwitz, S., 2020. The prevalence and significance of offset magma reservoirs at arc volcanoes. Geophys. Res. Lett. 47 https://doi.org/10.1029/2020GL087856 e2020GL087856.

Magee, C., Stevenson, C.T., Ebmeier, S.K., Keir, D., Hammond, J.O., Gottsmann, J.H., Whaler, K.A., Schofield, N., Jackson, C.A., Petronis, M.S., O'Driscoll, B., 2018. Magma plumbing systems: a geophysical perspective. J. Petrol. 59 (6), 1217–1251. https://doi.org/10.1093/petrology/egy064.

McTigue, D.F., 1987. Elastic stress and deformation near a finite spherical magma body: resolution of the point source paradox. J. Geophys. Res. Solid Earth 92 (B12), 12931–12940. https://doi.org/10.1029/JB092iB12p12931.

Mogi, K., 1958. Relations between the eruptions of various volcanoes and the deformation of the ground surface around them. Bull. Earthq. Res. Insti. Univ. Tokyo 36, 99–134.

Muirhead, J.D., Fischer, T.P., Oliva, S.J., Laizer, A., van Wijk, J., Currie, C.A., Lee, H., Judd, E.J., Kazimoto, E., Sano, Y., Takahata, N., Tiberi, C., Foley, S.F., Dufek, J., Reiss, M.C., Ebinger, C.J., 2020. Displaced cratonic mantle concentrates deep carbon during continental rifting. Nature 582 (7810), 67–72. https://doi.org/10.1038/s41586-020-2328-3.

Muller, C., del Potro, R., Biggs, J., Gottsmann, J., Ebmeier, S.K., Guillaume, S., Cattin, P. H., Van der Laat, R., 2015. Integrated velocity field from ground and satellite geodetic techniques: application to Arenal volcano. Geophys. J. Int. 200 (2), 863–879. https://doi.org/10.1093/gji/ggu444.

Murcia, H., Borrero, C., Németh, K., 2019. Overview and plumbing system implications of monogenetic volcanism in the northernmost Andes' volcanic province. J. Volcanol. Geotherm. Res. 383, 77–87. https://doi.org/10.1016/j.jvolgeores.2018.06.013.

Newhall, C.G., Punongbayan, R. (Eds.), 1996. Fire and mud: eruptions and lahars of Mount Pinatubo, Philippines,1126. Philippine Institute of Volcanology and Seismology, Quezon City.

Petibon, C.M., Kjarsgaard, B.A., Jenner, G.A., Jackson, S.E., 1998. Phase relationships of a silicate-bearing natrocarbonatite from Oldoinyo Lengai at 20 and 100 MPa. J. Petrol. 39 (11–12), 2137–2151.

Reilinger, R., McClusky, S., Vernant, P., Lawrence, S., Ergintav, S., Cakmak, R., Ozener, H., Kadirov, F., Guliev, I., Stepanyan, R., Nadariya, M., 2006. GPS constraints on continental deformation in the Africa-Arabia-Eurasia continental collision zone and implications for the dynamics of plate interactions. J. Geophys. Res. Solid Earth 111 (B5). https://doi.org/10.1029/2005JB004051.

Reiss, M.C., Muirhead, J.D., Laizer, A.S., Link, F., Kazimoto, E.O., Ebinger, C.J., Rümpker, G., 2021. The impact of complex volcanic plumbing on the nature of seismicity in the developing magmatic Natron Rift, Tanzania. Front. Earth Sci. 8, 609805. https://doi.org/10.3389/feart.2020.609805.

Reiss, M.C., De Siena, L., Muirhead, J.D., 2022. The interconnected magmatic plumbing system of the Natron Rift. Geophys. Res. Lett. 49, 1–11 e2022GL098922.

Roecker, S., Ebinger, C., Tiberi, C., Mulibo, G., Ferdinand-Wambura, R., Mtelela, K., Kianji, G., Muzuka, A., Gautier, S., Albaric, J., Peyrat, S., 2017. Subsurface images of the Eastern Rift, Africa, from the joint inversion of body waves, surface waves and gravity: investigating the role of fluids in early-stage continental rifting. Geophys. J. Int. 210 (2), 931–950. https://doi.org/10.1093/gji/ggx220.

Rosen, P.A., Gurrola, E., Sacco, G.F., Zebker, H., 2012. The InSAR scientific computing environment. In: Proc. EUSAR, pp. 730–733. Nuremberg, Germany.

Saria, E., Calais, E., Altamimi, Z., Willis, P., Farah, H., 2013. A new velocity field for Africa from combined GPS and DORIS space geodetic solutions: Contribution to the definition of the African reference frame (AFREF). J. Geophys. Res. Solid Earth 118, 1677–1697. https://doi.org/10.1002/jgrb.50137.

Saria, E., Calais, E., Stamps, D.S., Delvaux, D., Hartnady, C.J.H., 2014. Present-day kinematics of the East African Rift. J. Geophys. Res. Solid Earth 119 (4), 3584–3600. https://doi.org/10.1002/2013JB010901.

Segall, P., 2019. Magma chambers: what we can, and cannot, learn from volcano geodesy. Phil. Trans. R. Soc. A 37, 20180158. https://doi.org/10.1098/rsta.2018.0158.

Sigmundsson, F., Einarsson, P., Bilham, R., 1992. Magma chamber deflation recorded by the Global Positioning System: the Hekla 1991 eruption. Geophys. Res. Lett. 19 (14), 1483–1486. https://doi.org/10.1029/92GL01636.

Stamps, D.S., Calais, E., Saria, E., Hartnady, C., Nocquet, J.M., Ebinger, C.J., Fernandes, R.M., 2008. A kinematic model for the East African Rift. Geophys. Res. Lett. 35, L05304. https://doi.org/10.1029/2007GL032781.

Stamps, D.S., Saria, E., Ji, K.H., Jones, J.R., Ntambila, D., Daniels, M., Mencin, D., 2016a. TZVOLCANO - OLO1-OLO1_OLO_TZA2016 P.S., UNAVCO, GPS/GNSS Observations Dataset. https://doi.org/10.7283/T5TB15P4.

Stamps, D.S., Saria, E., Ji, K.-H., Jones, J.R., Ntambila, D., Daniels, M., Mencin, D., 2016b. TZVOLCANO - OLO2-OLO2_OLO_TZA2016 P.S., UNAVCO, GPS/GNSS Observations Dataset. https://doi.org/10.7283/T5JS9P7J.

Stamps, D.S., Saria, E., Ji, K.-H., Jones, J.R., Ntambila, D., Daniels, M., Mencin, D., 2016c. TZVOLCANO - OLO3-OLO3_OLO_TZA2016 P.S., UNAVCO, GPS/GNSS Observations Dataset. https://doi.org/10.7283/T5Z31XFX.

Stamps, D.S., Saria, E., Ji, K.-H., Jones, J.R., Ntambila, D., Daniels, M., Mencin, D., 2016d. TZVOLCANO - OLO4-OLO4_OLO_TZA2016 P.S., UNAVCO, GPS/GNSS Observations Dataset. https://doi.org/10.7283/T55M64H7.

Stamps, D.S., Saria, E., Ji, K.-H., Jones, J.R., Ntambila, D., Daniels, M., Mencin, D., 2016e. TZVOLCANO - OLO5-OLO5_OLO_TZA2016 P.S., UNAVCO, GPS/GNSS Observations Dataset. https://doi.org/10.7283/T5PK0DX.

Stamps, D.S., Saria, E., Ji, K.H., Jones, J.R., Ntambila, D., Daniels, M.D., Mencin, D., 2016f. Real-time data from the Tanzania Volcano Observatory at the Ol Doinyo Lengai volcano in Tanzania (TZVOLCANO). UCAR/NCAR - EarthCube. https://doi.org/10.5065/D6P849BM.

Stamps, D.S., Saria, E., Ji, K.-H., Jones, J.R., Ntambila, D., Daniels, M., Mencin, D., 2017a. TZVOLCANO - OLO6-OLO6_OLO_TZA2017 P.S., UNAVCO, GPS/GNSS Observations Dataset. https://doi.org/10.7283/T51V5CR2.

Stamps, D.S., Saria, E., Ji, K.-H., Jones, J.R., Ntambila, D., Daniels, M., Mencin, D., 2017b. TZVOLCANO - OLO7-OLO7_OLO_TZA2017 P.S., UNAVCO, GPS/GNSS Observations Dataset. https://doi.org/10.7283/T5F47MW0.

Stamps, D.S., Saria, E., Ji, K.-H., Jones, J.R., Ntambila, D., Daniels, M., Mencin, D., 2017c. TZVOLCANO - OLO8-OLO8_OLO_TZA2017 P.S., UNAVCO, GPS/GNSS Observations Dataset. https://doi.org/10.7283/T59C6W64.

Stamps, D.S., Saria, E., Ji, K.-H., Jones, J.R., Ntambila, D., Daniels, M., Mencin, D., 2021a. Tanzania Volcano Observatory - OLO9-OLO9_OLO_TZA2021 P.S., UNAVCO, GPS/GNSS Observations Dataset. https://doi.org/10.7283/EW7F-Z179.

Stamps, D.S., Kreemer, C., Fernandes, R., Rajaonarison, T.A., Rambolamanana, G., 2021b. Redefining East African Rift System kinematics. Geology 49 (2), 150–155. https://doi.org/10.1130/G47985.1.

Tizzani, P., Battaglia, M., Castaldo, R., Pepe, A., Zeni, G., Lanari, R., 2015. Magma and fluid migration at Yellowstone Caldera in the last three decades inferred from InSAR, leveling, and gravity measurements. J. Geophys. Res. Solid Earth 120 (4), 2627–2647. https://doi.org/10.1002/2014JB011502.

Toraldo Serra, E.M., Delouis, B., Emolo, A., Zollo, A., 2013. Combining strong-motion, InSAR and GPS data to refine the fault geometry and source kinematics of the 2011, M w 6.2, Christchurch earthquake (New Zealand). Geophys. J. Int. 194 (3), 1760–1777. https://doi.org/10.1093/gji/ggt186.

Wang, H., Wright, T.J., 2012. Satellite geodetic imaging reveals internal deformation of western Tibet. Geophys. Res. Lett. 39 (7) https://doi.org/10.1029/2012GL051222.

Wang, H., Wright, T.J., Yu, Y., Lin, H., Jiang, L., Li, C., Qiu, G., 2012. InSAR reveals coastal subsidence in the Pearl River Delta, China. Geophys. J. Int. 191 (3), 1119–1128. https://doi.org/10.1111/j.1365-246X.2012.05687.x.

Weinstein, A., Oliva, S.J., Ebinger, C.J., Roecker, S., Tiberi, C., 2017. Fault- magma interactions during early continental rifting: seismicity of the Magadi- Natron-Manyara basins, Africa. Geochem. Geophys. Geosyst. 18 (10), 3662–3686. https://doi.org/10.1002/2017GC007027.

Williams, C.A., Wadge, G., 1998. The effects of topography on magma chamber deformation models: Application to Mt. Etna and radar interferometry. Geophys. Res. Lett. 25 (10), 1549–1552. https://doi.org/10.1029/98GL01136.

Wright, T.J., Parsons, B.E., Jackson, J.A., Haynes, M., Fielding, E.J., England, P.C., Clarke, P.J., 1999. Source parameters of the 1 October 1995 Dinar (Turkey) earthquake from SAR interferometry and seismic bodywave modelling. Earth Planet. Sci. Lett. 172 (1–2), 23–37. https://doi.org/10.1016/S0012-821X(99)00186-7.

Yunjun, Z., Fattahi, H., Amelung, F., 2019. Small baseline InSaR time series analysis: Unwrapping error correction and noise reduction. Comput. Geosci. 133, 104331 https://doi.org/10.1016/j.cageo.2019.104331.